Carbohydrate Polymers 358 (2025) 123491

Contents lists available at ScienceDirect

Carbohydrate Polymers

journal homepage: www.elsevier.com/locate/carbpol

Boron-doped silica/chitosan-based elastic three-dimensional sponge scaffold for bone regeneration

Zheng Lei [a,1], Chunchun Li [b,1], Zhengchao Yuan [a,1], Xinyi Wang [a], Guangfang Cai [a], Panpan Shang [c], Yue Zhao [a], Muhammad Rafique [d], Mohamed EL-Newehy [e], Meera Moydeen Adulhameed [e], Muhammad Shafiq [f,*], Liang Song [b,*], Hao Zheng [a,*], Xiumei Mo [a,c,**]

[a] State Key Laboratory for Modification of Chemical Fibers and Polymer Materials, Shanghai Engineering Research Center of Nano-Biomaterials and Regenerative Medicine, College of Biological Science and Medical Engineering, Donghua University, 201620 Shanghai, China
[b] Department of Stomatology, Shanghai Fifth People's Hospital, Fudan University, Shanghai 200240, China
[c] Institute of Biomaterials and Biomedicine, School of Food and Pharmacy, Shanghai Zhongqiao Vocational and Technical University, 3888 Caolang Rd., Shanghai 201514, China
[d] School of Biomedical Engineering and Med-X Research Institute, Shanghai Jiao Tong University, Shanghai 200240, China
[e] Department of Chemistry, College of Science, King Saud University, P.O. Box 2455, Riyadh 11451, Saudi Arabia
[f] Innovation Center of NanoMedicine (iCONM), Kawasaki Institute of Industrial Promotion, Kawasaki-ku, Kawasaki 210-0821, Japan

ARTICLE INFO

Keywords:
Sponge
Chitosan
Short silica nanofiber
Electrospinning
Bone regeneration

ABSTRACT

Bone regeneration is crucial for repairing irregular bone defects, restoring skeletal structure and function, and promoting healing following injury. Sponge scaffolds, characterized by their high porosity and mechanical strength, are considered as effective biomaterials for bone tissue repair. In this study, we fabricated flexible silica (SiO_2) nanofiber membranes using electrospinning, which contained different concentrations of boron ions (B^{3+}). These SiO_2 fibers further combined with chitosan (CS) to create three-dimensional (3D) sponge scaffolds. Scaffolds exhibited remarkable elastic memory in the hydrated state, thereby enabling them to conform perfectly to irregular-shaped bone defects upon implantation. Scaffold containing lower concentrations of boron ions (B^{3+}) (CS/SiO_2-B1), selected through *in vitro* assays, could synergistically release boron and silicon ions and promote the proliferation as well as migration of cells related to bone regeneration. CS/SiO_2-B1 scaffolds also showed significantly higher expression of angiogenesis- and osteogenesis-related genes *in vitro*. In a rat cranial defect model, CS/SiO_2-B1 scaffolds promoted *de novo* bone production 6 weeks post-implantation. Taken together, these 3D sponge scaffolds may have broad implications for bone tissue repair and potentially other bio-related disciplines.

1. Introduction

Bone defects not only cause pain, limited mobility, and disability but they also adversely influence the quality-of-life (QOL) of patients. While bone exhibit self-healing ability, trauma, tumor resection, or congenital diseases may result in an incomplete or delayed functional recovery of the bone tissues (Barbosa et al., 2023; Xue et al., 2022). Autografts, allografts, ceramics, and *in situ* injectable bone cements are widely used for bone tissue engineering (TE) albeit several limitations (Wang et al., 2022). Autografts are gold-standard treatment options, however inadequate number of donors and donor-site associated risks impede their full utility (Tang et al., 2021; Xue et al., 2024). On the other hand, an inherent brittleness of ceramics limit their application prospect (Wang & Chang, 2020). Moreover, traditional bone cement is an inert material with a dense structure, which can hinder the infiltration of osteoblasts as well as constrict the formation of blood vessels (Jakus et al., 2016;

* Corresponding authors.
** Correspondence to: X. Mo, Institute of Biomaterials and Biomedicine, School of Food and Pharmacy, Shanghai Zhongqiao Vocational and Technical University, 3888 Caolang Rd., Shanghai 201514, China.
E-mail addresses: shafiqdr786@yahoo.com (M. Shafiq), sky_songliang@hotmail.com (L. Song), zhenghao@dhu.edu.cn (H. Zheng), xmm@dhu.edu.cn (X. Mo).
[1] Z.L, C.L, and Z.Y. are co-first authors.

https://doi.org/10.1016/j.carbpol.2025.123491
Received 2 December 2024; Received in revised form 26 February 2025; Accepted 7 March 2025
Available online 11 March 2025

Padalhin et al., 2018). Consequently, the development of three-dimensional (3D) porous scaffolds with excellent mechanical properties, biocompatibility, and biological functionality has received considerable interest of the research community for bone TE (Wang et al., 2019; Yuan et al., 2024).

Porous scaffolds may provide an conducive environment for cell adhesion and proliferation (Chen et al., 2023; Cheng et al., 2022; Liu et al., 2022). Traditionally, natural and synthetic polymers are used for the fabrication of scaffolds for bone TE albeit an acute lack of osteogenic and angiogenic ability (Mao et al., 2018; Wang et al., 2023; Xu et al., 2022). Bioactive glass (BG) can accelerate bone regeneration *via* therapeutic ions release *e.g.*, calcium ions, phosphate ions, silicate ions, *etc.*). These therapeutic ions can promote bone regeneration *via* the stimulation of osteogenic cells (*e.g.*, osteoblasts and osteocytes). The combination of BG with a porous scaffold can endow the scaffold with osteogenic properties (Wang et al., 2019). Weng et al. fabricated 3D hybrid nanofiber sponge scaffold using electrospun poly(lactic acid-*co*-glycolic acid) (PLGA)-collagen-gelatin and strontium-copper (Sr—Cu) co-doped BG fibers (Weng et al., 2018). These scaffolds exhibited good potential for cranial tissue regeneration albeit structural collapse below 35 % strain. The weak mechanical properties of BG fibers may further lower mechanical properties of the sponges. By combining flexible bioactive ceramic fibers (*e.g.*, short SiO_2 fiber) with polymeric materials (*e.g.*, chitosan (CS)), it is possible to preserve the bioactivity of the inorganic materials while imparting the flexibility of BG fibers to the polymer matrix (Zhao et al., 2024). Therefore, the development of a 3D scaffold that integrate both components represents a promising approach for bone TE.

Notably, SiO_2 nanofibers with small diameter exhibit excellent biocompatibility and osteo-inductive ability. SiO_2 can release silicon ions (Si^{4+}), which may promote angiogenesis and induce *de novo* bone production (Wang, Yuan, et al., 2024, Chen et al., 2016). Moreover, the release of boron ions (B^{3+}) may promote angiogenesis and osteogenesis, while inhibit inflammatory response by suppressing Toll-like receptor (TLR) signaling pathway (Donoiu et al., 2018; Li et al., 2019; Najafabadi & Abnosi, 2016). Therefore, boron-containing SiO_2 nanofibers could promote osteogenic ability of scaffolds. Moreover, to obtain a stable sponge with high resilience, Yuan et al. incorporated gelatin short fibers (SF) into a sponge scaffold (Yuan et al., 2024). While scaffolds exhibited good osteogenic ability, they showed high dissolution rate, structural collapse, and marginal antibacterial and anti-inflammatory functions. The CS, as a natural polymer, exhibits good biocompatibility, antimicrobial ability, and anti-inflammatory response (Ke et al., 2021; Rabea et al., 2003). It can form a stable 3D structure through chemical crosslinking, thereby providing excellent mechanical properties and creating a conducive environment for cell attachment (Fig. 1b) (Sukpaita et al., 2021; Wang et al., 2019).

We hypothesized that short flexible SiO_2 nanofibers integrated into CS can help obtain 3D integrated scaffolds with physical and mechanical properties higher than that of the pristine CS. We employed sol-gel electrospinning method to fabricate boron-doped flexible SiO_2 nanofiber membranes (SiO_2-B MF). These membranes were homogenized to obtain SF and then mixed with CS solution. By chemically cross-linking the CS and using freeze-drying technology, all components were fabricated into a 3D scaffold (Fig. 1a). We characterized the morphological structure, mechanical properties, and other physicochemical characteristics of the sponge scaffold, as well as evaluated biological properties *in vitro*, including angiogenesis and coagulation functions. Additionally, we evaluated *in vivo* osteogenic performance of the sponge scaffold in a rat cranial defect model.

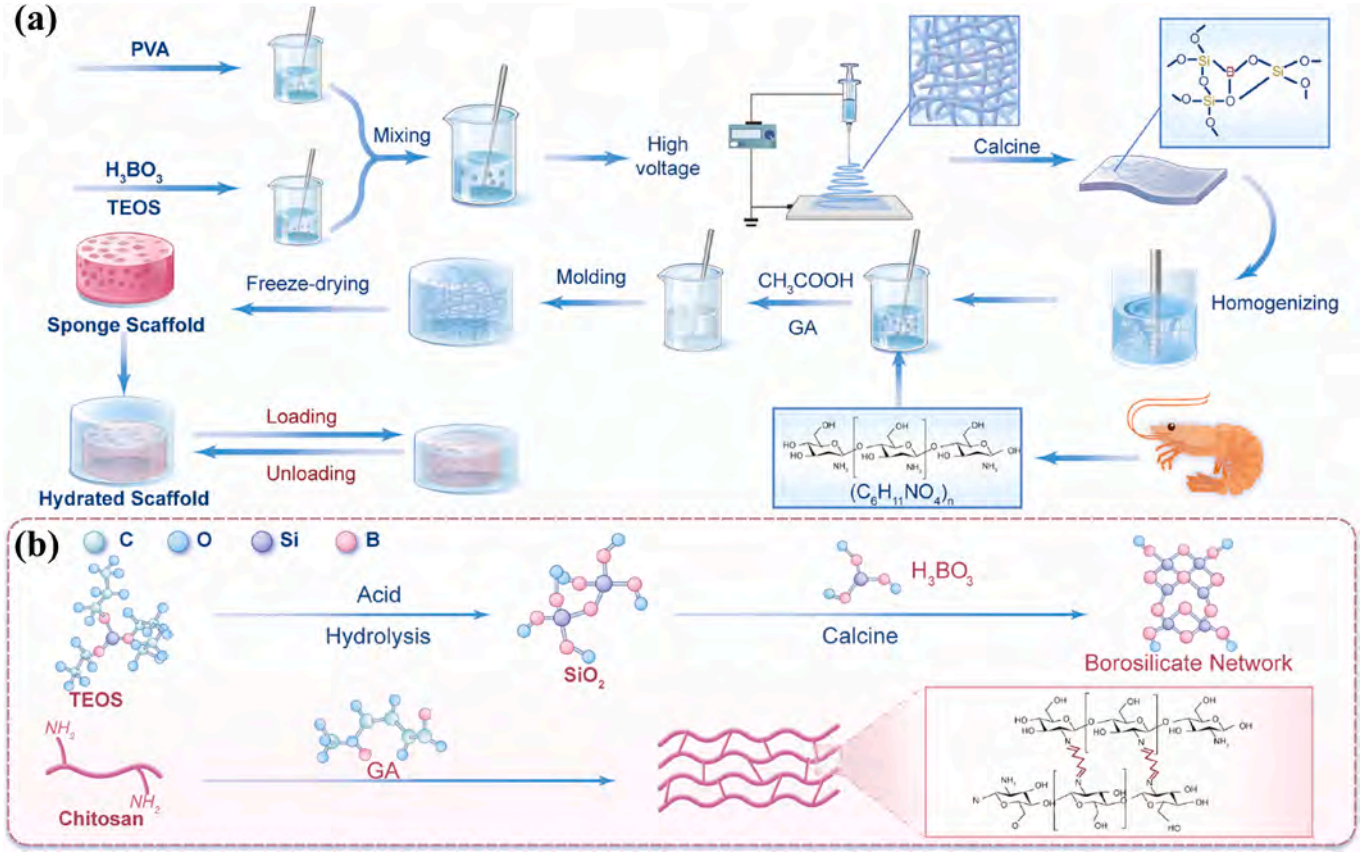

Fig. 1. Schematic illustration of the preparation of sponge scaffolds. (a) Fabrication of scaffolds. (b) Schematic diagram showing the synthesis of borosilicate networks and the crosslinking of chitosan during the fabrication of scaffolds.

2. Materials and methods

2.1. Materials

Boric acid (H_3BO_3), tetraethyl orthosilicate (TEOS), chitosan (CS, Mw = 70 kDa, degree of deacetylation ≥95 %, viscosity, 100–200 mPa. s), and poly(vinyl alcohol) (PVA, M_n = 86 kDa) were purchased from Aladdin (Shanghai, China). Citric acid (CA) and glutaraldehyde (GA) were obtained from Shanghai McLean Biochemical Technology Co., Ltd. (Shanghai, China). All chemicals were of analytical grade and used without any further purification.

2.2. Preparation of 3D sponge scaffold

2.2.1. Preparation of electrospun nanofiber membranes

1.0 g of PVA was dissolved in 10.0 mL of deionized water to obtain 10 % (*w/v*) solution. TEOS/deionized water/citric acid mixture (1:1:0.03, v/v) was prepared and stirred at room temperature (RT). Thereafter, different proportions of boric acid (H_3BO_3, molar ratios of H_3BO_3 to TEOS; 1:100, 1.5:100, and 3:100, respectively.) were dissolved in TEOS/deionized water/citric acid mixture and stirred for 8 h. PVA and H_3BO_3 solvates were blended at 1:1 weight ratio and stirred at RT for 10 h. Electrospun membranes were fabricated using following parameters: applied voltage, 16 kV; flow rate, 1.0 mL h^{-1}; collector, a rotating roller covered with nonwoven fabrics; and spinneret-to-collector distance, 15 cm. Electrospun fibers were calcined at 800 °C for 2 h to remove PVA. Membranes with different content of H_3BO_3 were represented as SiO_2-B1 FM (molar ratios of H_3BO_3 to TEOS, 1:100), SiO_2-B2 FM (molar ratios of H_3BO_3 to TEOS, 1.5:100), and SiO_2-B3 FM (molar ratios of H_3BO_3 to TEOS, 3:100).

2.2.2. Fabrication of sponge scaffolds

A total 0.875 g of CS was dissolved in 100 mL of 1 % (*v*/v) acetic acid solution to obtain a clear CS solution. Nanofiber membranes with varying boron content (ca. 1.625 g) were cut into 1 × 1 cm pieces and dispersed in the CS solution (Wang et al., 2019). The mixture was then homogenized at 10,000 rotations per minute (rpm) for 10 min with a high-speed homogenizer (IKA T18, Germany) to achieve uniform fibers dispersion (nanofibers: CS = 65:35, *w*/w). Thereafter, 0.875 mL of 1 wt % glutaraldehyde (GA) solution was added to the fiber dispersions with vigorous stirring for up to 10 min for cross-linking. The dispersion was poured into molds and frozen at −80 °C. CS/SiO_2-B sponge scaffolds were obtained after freeze-drying for up to 48 h with a freeze dryer (Shiv Instruments Technology Co., Ltd., Shanghai, China). Scaffolds were washed three times with anhydrous ethanol to remove the residual GA, and were again freeze-dried. Sponges prepared with SiO_2-B1 FM were indicated as CS/SiO_2-B1, while the other sponges were named as CS/SiO_2-B2, and CS/SiO_2-B3.

2.3. Characterization of electrospun nanofiber membranes and sponge scaffolds

2.3.1. Morphological analysis

The morphology of SiO_2-B FMs before and after calcination was observed by scanning electron microscope (SEM, Hitachi, TM-1000, Tokyo, Japan). Similarly, the morphology of SiO_2 fibers and CS/SiO_2-B scaffolds was examined. Fiber diameter was analyzed by using Nano Measurer software.

2.3.2. Structural analysis of sponge scaffolds

The distribution of different types of elements, such as silicon (Si), boron (B), carbon (C), nitrogen (N), and oxygen (O) in the CS/SiO_2-B scaffolds was studied with energy-dispersive spectroscopy (EDS). Structural analysis of scaffold was carried out with Fourier-transform infrared spectroscopy (FTIR, Thermo Fisher Scientific, USA) in the range of 2500–500 cm^{-1}. Thermal stability of scaffolds was assessed with a thermogravimetric analyzer (PerkinElmer Corporate Management Co., Ltd., TGA8000, Shanghai, China) in an air environment and the temperature was in range of 25 °C for up to 800 °C with a heating rate of 5 °C per minute.

2.3.3. Mechanical properties

Mechanical properties of the scaffolds were evaluated in dry and wet conditions using a universal tensile testing machine (Instron 5567, Norwood, MA) and 200 N load cell (Transcell Technology, Inc., BAB-20MT, USA). The temperature for the measurement of mechanical properties was 25 °C and relative humidity was approximately 44 %. The protruding portions on the upper and lower surfaces of the scaffold were removed using a surgical scalpel to prepare standard cylindrical samples (diameter, 11 mm and height 14 mm). Upper and lower surfaces of the scaffold were fixed. Compression tests were performed on the samples at a constant rate of 2 mm/min for up to 80 % strain. Compressive moduli and ultimate compressive strength (UCS) of scaffolds were calculated from the compression curves (n = 6). Fatigue tests were performed at a scan rate of 2 mm/min and a compressive strain of 60 % for 1, 50, and 100 cycles.

2.3.4. Density and water absorption

The diameter (d), height (h), and weight (A_0) of the dry scaffolds (n = 6) were measured, and the density of the scaffolds was calculated by Eq. (1):

$$\text{Density} = \frac{A_0}{\pi \times (d/2)^2 \times h} \quad (1)$$

Scaffolds were then fully immersed in deionized water at 25 °C for 20 min to achieve saturation. The surface of the scaffolds was gently wiped with filter paper, and samples were weighed again (A_t). The water absorption capacity of scaffolds was calculated by Eq. (2):

$$\text{Water absorption capacity (\%)} = \frac{A_t - A_0}{A_0} \times 100\% \quad (2)$$

2.3.5. Degradation of scaffolds

Dry scaffolds (n = 6 per group) were weighed (B_0) and incubated in 0.9 % phosphate-buffered saline (PBS) at 100 rotations per minute (rpm) and 37 °C. Samples were collected, rinsed with deionized water, freeze-dried, and weighed (B_t) at pre-determined time points. Degradation rate of scaffolds was calculated by Eq. (3).

$$\text{Remained mass (\%)} = \frac{B_t}{B_0} \times 100\% \quad (3)$$

where B_0 and B_t show the weight of samples at t = 0 and t = t, respectively.

2.3.6. Release of therapeutic ions from sponge scaffolds

Scaffolds (weight, 25 mg, n = 3) were incubated in 0.9 % NaCl solution at 37 °C. At pre-determined time points, a portion of the solution was collected, and an equal volume of fresh 0.9 % NaCl solution was added. The collected solutions were analyzed using inductively-coupled plasma atomic emission spectroscopy (ICP-AES, Prodigy Plus, Leeman, USA) to delineate the release of silicon ions (Si^{4+}) and boron ions (B^{3+}).

2.4. Cytocompatibility of sponge scaffolds

2.4.1. Cell viability and proliferation

The viability as well as proliferation of human umbilical vein endothelial cells (HUVECs), mouse embryonic pre-osteoblast cells (MC3T3-E1), and rat bone marrow-derived mesenchymal stem cells (rBMSCs) were evaluated using different types of scaffolds. HUVECs were cultured in DMEM, while MC3T3-E1 and rBMSCs were grown in α-MEM. Both media were supplemented with 1 % penicillin/streptomycin and 10 % fetal bovine serum (FBS). Scaffolds were cut into thin

slices (thickness, 1 mm) and sterilized by ultraviolet (UV) irradiation on both sides for up to 12 h. Sterilized scaffolds ($n = 4$) were placed in a 48-well cell culture plate, secured with sterilized stainless-steel rings, and 600 μL of the corresponding complete medium was added into each well. Scaffolds were incubated at 37 °C and 5 % CO_2 for 30 min. HUVECs, MC3T3-E1, and rBMSCs were seeded on scaffolds (cell density $= 2 \times 10^4$ cells/well) and cultured for 1, 3, and 5 days in an incubator. Cell proliferation was evaluated with cell counting kit-8 (CCK-8) assay at day 1, 3, and 5. Briefly, culture medium was aspirated and 200 μL of CCK-8 working solution (serum-free medium: CCK-8 solution = 9:1, *v*/v) was added into each well, followed by incubation for 1 h and 30 min. Approximately, 100 μL of solution was collected from each well and absorbance was measured at 450 nm with a microplate reader (Thermo Fisher Multiskan FC, Thermo Fisher Scientific, Waltham, MA, USA). Live/dead staining was performed using calcein-AM and propidium iodide (PI) and cells were imaged with a fluorescence microscope (DMi, Leica, Germany). HUVECs, MC3T3-E1, and rBMSCs were cultured on sterilized scaffolds in the same manner for up to 5 days. DAPI/F-actin staining was performed for cell cytoskeletal staining and imaging was performed with a fluorescence microscope.

2.4.2. Transwell migration assay

The migration of HUVECs, MC3T3-E1, and rBMSCs was evaluated with a Transwell migration assay. Scaffolds were cut into thin slices and sterilized with ultraviolet (UV) light for up to 24 h. Subsequently, slices were soaked in culture medium for 48 h (approximately 25 mg of scaffolds were immersed in 10 mL of culture medium). Extract solution from various scaffolds was filtered with a syringe. Transwell chambers were placed in a 24-well cell culture plate. 200 μL of cell suspension was added into inserts ($n = 3$, 2×10^5 cells/well), and 800 μL of the extract solution from different scaffolds was added into wells. Plates were incubated at 37 °C for 12 h. Cells were fixed with 4 % paraformaldehyde (PFA) for 30 min and stained with 100 μL of 1 % crystal violet solution for 5 min. Cells on the upper side of the membranes were carefully removed with a moist cotton swab, cells on the bottom side of membranes were observed with an optical microscope (Eclipse Nikon, Japan).

2.5. Angiogenic effects of sponge scaffolds

2.5.1. Scratch wound healing assay

Extract solution of different types of scaffolds was collected as described in section 2.4.2. HUVECs were cultured in a 24-well cell culture plate ($n = 3$, 3×10^4 cells/well) and grown for up to 90 % confluence. A sterile 200 μL pipette was used to establish a uniform scratch across cell monolayer. Cells were washed with PBS to remove debris, and 1 mL of extract solution (containing 1 % FBS) was added into each well. Cell migration was observed at $t = 0$ and $t = 24$ h with an optical microscope. Cell migration rate was calculated by Eq. (4), based on the scratch area at $t = 0$ (P_0) and $t = 24$ h (P_t).

$$\text{Migration rate} = \frac{P_t}{P_0} \times 100\% \quad (4)$$

2.5.2. Angiogenesis-related genes in vitro

The expression of angiogenesis-related genes in HUVECs was detected by quantitative real-time PCR (qRT-PCR), including vascular endothelial growth factor (VEGF), kinase insert domain receptor (KDR), and endothelial nitric oxide synthase (eNOS). Briefly, HUVECs were seeded in a 6-well plate and cultured for up to confluence ($n = 3$, 3×10^5 cells/well). Extract solution of different scaffolds was collected as described in section 2.4.2. The medium was then replaced with the extraction solution of different scaffolds, and cells were cultured until day 5. Cells cultured in the standard medium were used as a negative control. Total RNA was extracted from cells using a TRIzol reagent. The harvested RNA was reverse transcribed into cDNA using the RevertAid First Strand cDNA Synthesis Kit (Thermo Fisher Scientific). qRT-PCR was performed using NovoStart® SYBR qPCR SuperMix Plus (Novoprotein Scientific Inc., Shanghai, China) on an Applied Biosystems™ 7500 Real-Time PCR System. Gene expression levels were normalized to the housekeeping gene glyceraldehyde 3-phosphate dehydrogenase (GAPDH). The primers used in this study are shown in Table S1.

2.5.3. Tube formation in vitro

The matrix (catalog no. 356234, BD Matrigel, USA) was thawed at 4 °C and subsequently spread onto a 48-well cell culture plate (100 μL/well), followed by incubation at 37 °C for 20 min for solidification. Extract solution of different types of scaffolds was collected as described in section 2.4.2. HUVECs were seeded into the Matrigel-coated wells ($n = 3$, 2×10^4 cells/well), and 200 μL of extract solution of different scaffolds was added. The cells were cultured in the incubator for 4 h, during which they began to migrate, extend, and form capillary-like structures. The formation of the vascular structures was observed using an optical microscope. ImageJ was utilized to analyze parameters related to angiogenesis, including junctions, meshes, and master segments.

2.6. Osteogenic effects of sponge scaffolds

2.6.1. Alkaline phosphatase activity and alizarin red S staining

Osteogenic induction medium was prepared using α-MEM (supplemented with 10 % FBS, 1 % penicillin-streptomycin, 10 mM β-glycerophosphate, 50 μg/mL ascorbic acid, and 10^{-8} M dexamethasone). Extract solution of different scaffolds was collected as described in section 2.4.2. Extract solution from different types of scaffolds was then mixed with the osteogenic induction medium in equal volumes to prepare the osteogenic induction medium containing the scaffold extract. rBMSCs were seeded in a 48-well cell culture plates and cultured until confluence (n = 3, 2×10^4 cells/well), after which the medium was replaced with the osteogenic induction medium and cells were cultured for 7 and 14 days. For alkaline phosphatase (ALP) staining, rBMSCs were stained using a 5-bromo-4-chloro-3-indolyl phosphate/ Nitro Blue Tetrazolium (BCIP/NBT) analysis kit and observed under an optical microscope. For ALP quantification, cells were lysed using a cell lysis buffer at day 7 and 14, and total protein concentration was determined with a Bicinchoninic Acid (BCA) assay kit (Beyotime Biotechnology Co., Ltd., Shanghai, China), followed by ALP concentration measurement using an ALP assay kit. ALP activity was then calculated. For Alizarin Red S (ARS) staining, rBMSCs were cultured for up to 7 and 14 days similar to the above-mentioned procedure, after which the cells were fixed using 4 % PFA for 20 min. 2 % ARS working solution was added into the wells for staining for 10 min, followed by washing with DI water three times to remove unbound dye. Imaging was performed with an optical microscope. For ARS quantification, 200 μL of 10 % acetic acid solution was added into each well, incubated at RT for 2 h to dissolve calcium salt deposits, and absorbance was measured at 405 nm using a microplate reader.

2.6.2. Osteogenic-related genes in vitro

The expression of osteogenesis-related genes in rBMSCs, including osteopontin (OPN), osteocalcin (OCN), runt-related transcription factor 2 (RUNX2), and collagen type I (COL-I) was detected by qRT-PCR. Briefly, rBMSCs were seeded in a 6-well cell culture plate and cultured for up to confluency ($n = 3$, 2×10^4 cells/well). The preparation methods of the extract solution of different types of scaffolds as well as the composition of osteogenesis induction medium without scaffold extract are described in section 2.6.1. Subsequently, the medium was replaced with an osteogenic induction medium containing extract solution from various scaffolds (osteogenic induction medium: scaffold extract = 1:1, *v*/v) and cells were cultured for up to day 14. qRT-PCR was performed following the method used for the analysis of angiogenesis-related genes in section 2.5.2. The primers used in this

study are listed in Table S2 (Supporting Information).

2.7. Hemostatic ability of sponge scaffolds

2.7.1. Blood clotting assay

For hemostatic ability of scaffolds, a dynamic whole-blood coagulation assay was performed. CS/SiO_2, CS/SiO_2-B1, CS/SiO_2-B2, and CS/SiO_2-B3 scaffolds were cut into thin slices (diameter = 11 mm, height = 1 mm, $n = 3$) and incubated at 37 °C for 5 min. 100 μL of fresh anticoagulated rabbit whole blood (supplemented with 10 % sodium citrate) was added to the scaffolds followed with the dropwise addition of 10 μL of calcium chloride ($CaCl_2$, 0.2 M) solution. Samples were then incubated at 37 °C for 10 min for blood coagulation. Thereafter, 10 mL of deionized (DI) water was added to the samples and they were shaken in an orbital shaker at 37 °C for 5 min to remove any unbound blood. The absorbance of the supernatant was measured at 540 nm (D_t). Deionized water and 0.9 % NaCl were used as positive (D_m) and negative controls (D_n), respectively. The blood coagulation index (BCI) was calculated by Eq. (5).

$$\mathrm{BCI} = \frac{D_t - D_n}{D_m - D_n} \times 100\% \tag{5}$$

2.7.2. Hemocompatibility of sponge scaffolds

Fresh anticoagulated rabbit whole blood (10 % sodium citrate) was centrifuged at 1300 rpm for 15 min. The precipitated RBCs were collected and washed three times with saline. CS/SiO_2, CS/SiO_2-B1, CS/SiO_2-B2, and CS/SiO_2-B3 scaffolds (weight, 5 mg, $n = 3$) were placed into a 2 mL of centrifuge tubes and 800 μL of 0.9 % NaCl was added. Samples were incubated at 37 °C for 10 min, followed by the addition of 200 μL of diluted RBCs (RBCs: 0.9 % NaCl = 1:50, *v/v*) into each tube and gentle mixing. After incubation at 37 °C for 30 min, samples were centrifuged at 3000 rpm for 10 min, and the absorbance of the supernatant was measured at 540 nm (I_t). Deionized water and 0.9 % NaCl were used as positive (I_m) and negative controls (I_n), respectively. The hemolysis ratio of the samples was calculated by Eq. (6).

$$\text{Hemolysis ratio } (100\%) = \frac{I_t - I_n}{I_m - I_n} \times 100\% \tag{6}$$

2.8. Antibacterial activity of sponge scaffolds

The antimicrobial activity of the scaffold was evaluated with Gram-positive bacteria *Staphylococcus aureus* (*S. aureus*) and Gram-negative bacteria *Escherichia coli* (*E. coli*). Briefly, bacterial cultures were inoculated in a liquid bacterial growth medium (LB Broth) until reaching a bacterial concentration of 10^8 colony-forming units per milliliter (CFU/mL). CS/SiO_2, CS/SiO_2-B1, CS/SiO_2-B2, and CS/SiO_2-B3 (4 mg, $n = 6$) were co-cultured with the diluted bacterial solution (bacterial solution: PBS = 1:1000, v/v) for 24 h. After co-culturing, the bacterial solution was further diluted with PBS (bacterial solution: PBS = 1:1000, v/v), evenly spread and inoculated onto Luria-Bertani agar plates and incubated at 37 °C for 12 h. The bacteria were photographed and the colonies were counted. After co-culturing, the bacterial suspension was centrifuged to collect the bacteria, which were then resuspended in 2.5 % glutaraldehyde solution and fixed overnight at 4 °C. The bacterial morphology was subsequently observed using an electron microscope. The bacterial solution co-cultured without the scaffold served as the control.

2.9. Anti-inflammatory and antioxidant capacity of sponge scaffolds

Anti-inflammatory and antioxidant properties of the sponge scaffold were evaluated using extract solution of different types of scaffolds. The detailed procedure about the collection of extract solution of scaffolds is described in section 2.4.2. RAW 264.7 macrophages were seeded into 6-well plates and cultured for 12 h ($n = 3{,}3 \times 10^6$ cells/well).Thereafter, original medium was discarded, and 1 mL of complete medium containing 100 ng/mL lipopolysaccharide (LPS) was added into each well for 8–12 h to induce the polarization of RAW 264.7 macrophages. LPS-containing medium was then replaced with an equal volume of scaffold extract and incubated for 24 h. Antioxidant activity of scaffolds was delineated with 2′,7′-dichlorodihydrofluorescein diacetate (DCFH-DA) assay kit (Beyotime Biotechnology Co., Ltd., Shanghai, China) and intracellular levels of reactive oxygen species (ROS) were measured. ROS clearance was observed using a fluorescence microscope, and quantification was performed with a CytoFLEX flow cytometer (Becton Dickinson, USA).

RAW264.7 macrophages culture was performed for the detection of immune cell immune phenotypes. Cells were collected by centrifugation from scaffolds' extract, and nitric oxide (NO) level in the supernatant were measured with a NO detection kit (Beyotime Biotechnology Co., Ltd., Shanghai, China). Cell pellet was resuspended in 1 mL PBS containing 1 μg of Fluorescein Isothiocyanate (FITC) anti-mouse CD86 antibody and 0.4 μg of FITC anti-mouse CD206 antibody (BioLegend) on ice for 30 min under light protection. Cells were washed with PBS two times to remove non-specifically bound antibodies and the expression of CD86 and CD206 was analyzed using a flow cytometer. The obtained data was processed with FlowJo software (FlowJo V 10) ($n = 3$).

2.10. Animal experiments

Animal procedures were carried out in accordance with the guidelines of the Animal Care Committee of Shanghai Fifth People's Hospital, affiliated with Fudan University (Approval No. 2024-DWYY-038) in accordance with the National Research Council's Guide for the Care and Use of Laboratory Animals. Male SD rats (weight; 200 g; age, 6 weeks) were used for *in vivo* studies, three groups of scaffolds, with each group containing eight specimens.. Briefly, the cranial area of rats was disinfected and shaved. A circular cutting drill was used to create a 5 mm diameter bone defect on both sides of the top of the skull. CS/SiO_2 or CS/SiO_2-B1 scaffolds were sterilized with irradiation for sterilization, (diameter, 5 mm and thickness, 0.7 mm) were inserted into the defect site, and the skin incisions were closed. Defects without any treatment were used as controls. At 3 and 6 weeks post-operatively, cranial bone tissues were collected and fixed in 4 % PFA. Micro-CT was used to analyze an extent of bone defect repair as well as quantify various parameters of *de novo* bone formation. Bone tissues were subsequently decalcified, embedded in paraffin, and sectioned into thin slices. Histological analysis of explanted samples was performed using Hematoxylin and Eosin (H&E) and Masson's Trichrome (MT) staining. Tissue sections were incubated in a 5 % bovine serum albumin (BSA) solution for 1 h to block nonspecific binding, followed by incubation in primary antibody solutions (anti-OCN and anti-OPN) at 4 °C for 12 h. After removal of the primary antibodies, sections were immersed in a 3,3′-diaminobenzidine (DAB) solution for colour development.

2.11. Statistical analysis

In each experiment, the data collected from three or more repetitions were statistically analyzed using GraphPad Prism S (version 9.5.0). Significant differences were determined using one-way analysis of variance (ANOVA), with $^*p < 0.05$, $^{**}p < 0.01$, and $^{***}p < 0.001$ considered statistically significant.

3. Results

3.1. Fabrication and characterizations of sponge scaffolds

Flexible silica nanofibers containing different content of boric acid were successfully prepared by electrospinning following our previous report (Liu et al., 2022; Porrelli et al., 2021). Electrospun fibers were further calcined to obtain flexible boron-doped silica fibers. During

calcination, the boron from the boric acid can form a borosilicate network (Huang et al., 2024). The calcined nanofiber membranes exhibited white colour and good toughness, allowing them to be folded without distinct structural collapse (Fig. 2). SEM images showed that the nanofibers were smooth and uniform, without any signs of beads or rupture (Fig. 2b). Nanofiber membranes were further processed into SF with a homogenizer (Fig. 2c), which enhanced the dispersion of fibers in water as well as facilitated the subsequent assembly of fibers into 3D scaffolds.

Prior to calcination at 800 °C, the diameters of fibers containing PVA were measured and found to be 0.58 ± 0.17 μm, 0.57 ± 0.19 μm, 0.51 ± 0.16 μm, and 0.55 ± 0.19 μm for SiO_2 FM, SiO_2-B1 FM, SiO_2-B2 FM, and SiO_2-B3 FM, respectively (Fig. 2g & Supporting Materials Fig. S1). On the other hand, post-calcination, the corresponding fiber diameters were reduced to 0.40 ± 0.10 μm, 0.44 ± 0.14 μm, 0.46 ± 0.13 μm, and 0.43 ± 0.12 μm for SiO_2 FM, SiO_2-B1 FM, SiO_2-B2 FM, and SiO_2-B3 FM, respectively (Fig. 2h-k). This decrease in nanofiber diameter following calcination can be attributed to the removal of PVA, which served as a sacrificial template. It is worth to note that the incorporation of boron did not significantly affect the fiber diameter as compared to pure SiO_2 nanofiber membranes.

The SF were uniformly mixed with CS and crosslinked with the GA. This mixture was then cast into a 48-well cell culture plate to obtain a light yellow, sponge scaffold (Fig. 2d). Varying boron content in the nanofiber membranes enabled the fabrication of different types of scaffolds, such as CS/SiO_2, CS/SiO_2-B1, CS/SiO_2-B2, and CS/SiO_2-B3. These scaffolds exhibited smooth surfaces and similar morphologies. However, pure CS scaffolds manifested poor structural integrity owing to the lack of short nanofibers. SEM images showed a multilayered stacked structure of scaffolds along with smooth pores albeit lack of a honeycomb-like structure (Fig. 2e). Magnified images further showed an absence of short nanofibers in the pure CS scaffolds, thereby resulting into a loose structure (Fig. 2f). In contrast, cross-sectional images of sponge scaffolds containing short nanofibers displayed a honeycomb-

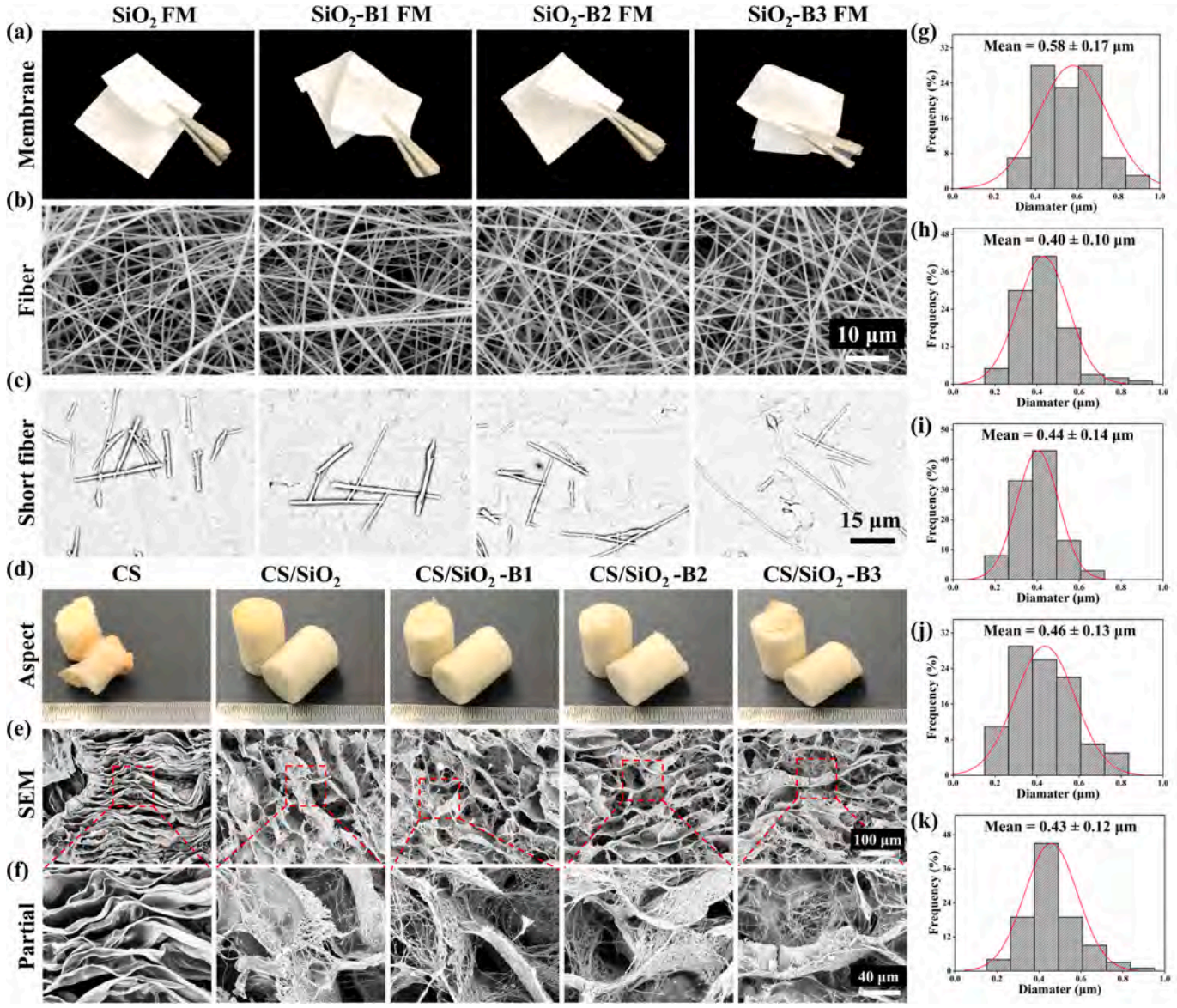

Fig. 2. Morphological analysis of electrospun fibers and scaffolds. (a) Macroscopic images of flexible nanofiber membranes. SEM images of nanofiber membranes with different boron content (b) and SF (c). Scale bars, 10 μm (b) and 15 μm (c). (d) Macroscopic images of pure CS scaffold as well as scaffolds containing boron-doped silica nanofibers. SEM images of sponge scaffolds at lower (e) and higher magnification (f). Scale bars, 100 μm (e) and 40 μm (f). (g) Statistical analysis of the fiber diameter of silica nanofibers before calcination. (h-k) Statistical analysis of the fiber diameters of SiO_2 FM, SiO_2-B1 FM, SiO_2-B2 FM, and SiO_2-B3 FM scaffolds after calcination.

like porous structure; short nanofibers were interconnected to provide a structural support as well as form pore walls in conjunction with the CS (Fig. 2e-f). This morphology of scaffolds closely recapitulated natural ECM morphological features; porous architecture, interconnected pores, and roughness of the nanofibers may promote cell attachment, infiltration, and neovascularization (Cai et al., 2024).

Thermal stability of scaffolds was analyzed using TGA (Supplementary Materials Fig. S3b). All scaffolds exhibited significant mass loss with an increase in the temperature. Initially, water was evaporated from the scaffolds, followed by the degradation of the CS, thereby leaving behind inorganic components, including silica (SiO_2) and boron oxide (B_2O_3). Consequently, the residual mass of the samples was increased with an increase in the boron content in the scaffolds. Elemental composition of the scaffolds was next ascertained with EDS, which revealed a uniform distribution of carbon (C), oxygen (O), silicon (Si), nitrogen (N), and boron (B) in CS/SiO_2-B1 scaffold (Fig. 3a). The density of boron was increased with an increase in the boron content in the membranes, as evidenced by enhanced fluorescence intensity of boron (Supplementary Materials Fig. S2). These results were further corroborated by the quantitative elemental analysis (Fig. 3d). Structural analysis of scaffolds was carried out with FTIR (Supplementary Materials Fig. S3a). FTIR spectra showed characteristic band at 800 cm^{-1} for CS/SiO_2, CS/SiO_2-B1, CS/SiO_2-B2, and CS/SiO_2-B3 scaffolds, which was attributed to the siloxane linkages (Si-O-Si) of the borosilicate network (Zheng et al., 2020). On the other hand, the bands at 1550 cm^{-1} and 1400 cm^{-1} were ascribed to the vibrational absorption of amide and methyl groups in CS (Afshar & Ghaee, 2016).

The four types of scaffolds exhibited lower density and high water absorption (Fig. 3e-f). The CS/SiO_2 scaffolds degraded slowly, with a residual weight of 68 % after 8 weeks of degradation *in vitro*. The residual weight of all scaffolds was approximately 79 % at week 4 after degradation *in vitro*. The degradation profiles of boron-doped scaffolds were comparable to that of CS/SiO_2 scaffolds, with no significant differences in the weight loss among the scaffolds (Fig. 3o). Morphological analysis of the CS/SiO_2-B1 scaffold during degradation at specific time points over 8 weeks revealed the collapse of its honeycomb-like structure as well as a reduction in the porous structures as the degradation was progressed (Fig. 3c). The weakening of the connections between short nanofibers, due to the gradual degradation of the CS component, led to the formation of stacked sheet-like structures, with no significant differences in degradation morphology between scaffolds (Supplementary Materials Fig. S4).

We examined the release of boron ions (B^{3+}) and silicon ions (Si^{4+}) from scaffolds in PBS *in vitro* (Fig. 3m-n). Both ions exhibited sustained release of therapeutic ions over 8 weeks. All boron-doped scaffolds showed similar release profiles of boron ions (B^{3+}), whereby the release of ions was correlated with the amount of boron incorporated into the scaffolds. Moreover, owing to the higher content of boron oxide (B_2O_3) in CS/SiO_2-B3 scaffold, more number of borosilicate networks were formed. These borosilicate networks (Si-O-B) are susceptible to hydrolysis. Consequently, scaffolds with higher boron content released more number of silicon ions (Si^{4+}) (Fig. 3n) (Zheng et al., 2020).

Mechanical properties of scaffolds were evaluated by compression testing (Fig. 3g). Under 80 % strain in the dry state, scaffolds maintained structural integrity. However, an irreversible shrinkage was observed in the scaffolds after compression (Supplementary Materials Fig. S5a). The incorporation of boron did not affect the ultimate compressive strength (UCS) or compressive moduli of scaffolds (Fig. 3h-i). Compression cycling tests performed on the scaffolds in the wet state demonstrated excellent fatigue resistance. Scaffolds were able to recover to their original height even after experiencing 60 % strain during cyclic compression (Fig. 3b). Although CS/SiO_2, CS/SiO_2-B1, CS/SiO_2-B2 and CS/SiO_2-B3 scaffolds were subjected to 100 compression cycles, they were still able to maintain their structural integrity (Fig. S5b). However, maximum stress of the scaffolds showed a significant reduction after 50 cycles (Fig. 3j-l). Unlike CS/SiO_2 scaffolds, pure CS scaffolds with relatively low content of CS exhibited weak mechanical properties under dry state. While CS scaffolds did not collapse in the wet state, they showed an expansion presumably due to the lack of the SF (Supplementary Materials Fig. S6).

3.2. Cytocompatibility of sponge scaffolds

The cytocompatibility of sponge scaffolds was assessed by growing HUVECs, MC3T3-E1, and rBMSCs on the scaffolds for up to 5 days *in vitro* (Fig. 4). Live/dead staining and CCK-8 assays were carried out to evaluate cell viability and cell proliferation (Fig. 4b, d-f). All cell types exhibited good proliferative activity and were uniform distributed on scaffolds. DAPI/F-actin staining revealed that some cells were also adhered to the fibrous pore walls of the sponge scaffold and exhibited a spindle-like morphology, which is indicative of cell migration within scaffold pores (Supplementary Materials Fig. S7). CCK-8 assay also showed cell proliferation in scaffolds over time. Boron-doped scaffolds manifested considerably higher cell proliferation as compared to the CS/SiO_2 group, which can be ascribed to the release of boron ions (B^{3+}) from the scaffolds. CS/SiO_2-B1 scaffold outperformed other boron-loaded scaffolds in terms of cell proliferation. It is worth to note that the cell density was decreased with an increase in boron content in the scaffolds, thereby indicating an inhibitory effect of the higher concentrations of boron ions (B^{3+}) for cell proliferation (Brown et al., 2008; Li et al., 2019). The effects of scaffolds on cell migration were evaluated using transwell migration (Fig. 4a). All scaffold groups enhanced cell migration compared to the control group (Fig. 4c). Interestingly, the CS/SiO_2-B1 and CS/SiO_2-B2 scaffolds facilitated higher cell migration than that of the other groups. Quantitative analsyis indicated that boron-doped scaffolds promoted cell migration more effectivelyas compared to the CS/SiO_2 scaffolds (Fig. 4g-i) These results indicated the beneficial effect of sponge scaffolds to promote cell survival and proliferation as well as cell migration *in vitro*.

3.3. Angiogenic effects of sponge scaffolds

Bioactive ions can promote cell migration, which may promote tissue repair (Yuan et al., 2022). The effects of scaffolds on cell migration were evaluated using a wound healing assay *in vitro* (Fig. 5a). The scaffold groups showed higher cell migration as compared to the control group, whereby optimal cell migration was observed in the CS/SiO_2-B1 group (Fig. 5b). Quantitative analysis of the scratches also revealed significantly rapid wound closure in the CS/SiO_2-B1 group than that of the other groups (Fig. 5d).

The pro-angiogenic effects of silicon ions (Si^{4+}) and boron ions (B^{3+}) released from scaffolds were assessed using a tube formation assay (Fig. 5a). As compared to the control group, HUVECs cultured along with the extract solution of different types of scaffolds formed a well-defined tubular network along with branch nodes and circular meshes after 6 h of incubation (Fig. 5c). Quantitative analysis indicated that the number of master segments were significantly higher in CS/SiO_2-B1 group than that of the other groups (9.0 ± 3.1, 21.0 ± 3.2, 17.0 ± 3.8, and 10.0 ± 2.0 in CS/SiO_2, CS/SiO_2-B1, CS/SiO_2-B2, and CS/SiO_2-B3 groups, respectively) (Fig. 5c-g). Boron-doped scaffolds exhibited more pronounced tubular structures, branching nodes and reticular circles than that of the CS/SiO_2, where the optimal effects were observed in the CS/SiO_2-B1 group. We further carried out qRT-PCR to gain further mechanistic insight into scaffolds-mediated angiogenesis and evaluated the expression of angiogenesis-related genes in HUVECs (Fig. 5a). Boron-loaded scaffolds significantly enhanced the mRNA expression of angiogenesis-related genes, including VEGF, KDR, and eNOS. CS/SiO_2-B1 group showed the highest expression of angiogenic genes than that of scaffolds with the higher boron content (*e.g.*, CS/SiO_2-B2, and CS/SiO_2-B3)(Fig. 5h-j). These results showed that the released silicon ions (Si^{4+}) and boron ions (B^{3+}) can synergistically promote blood vessel regeneration.

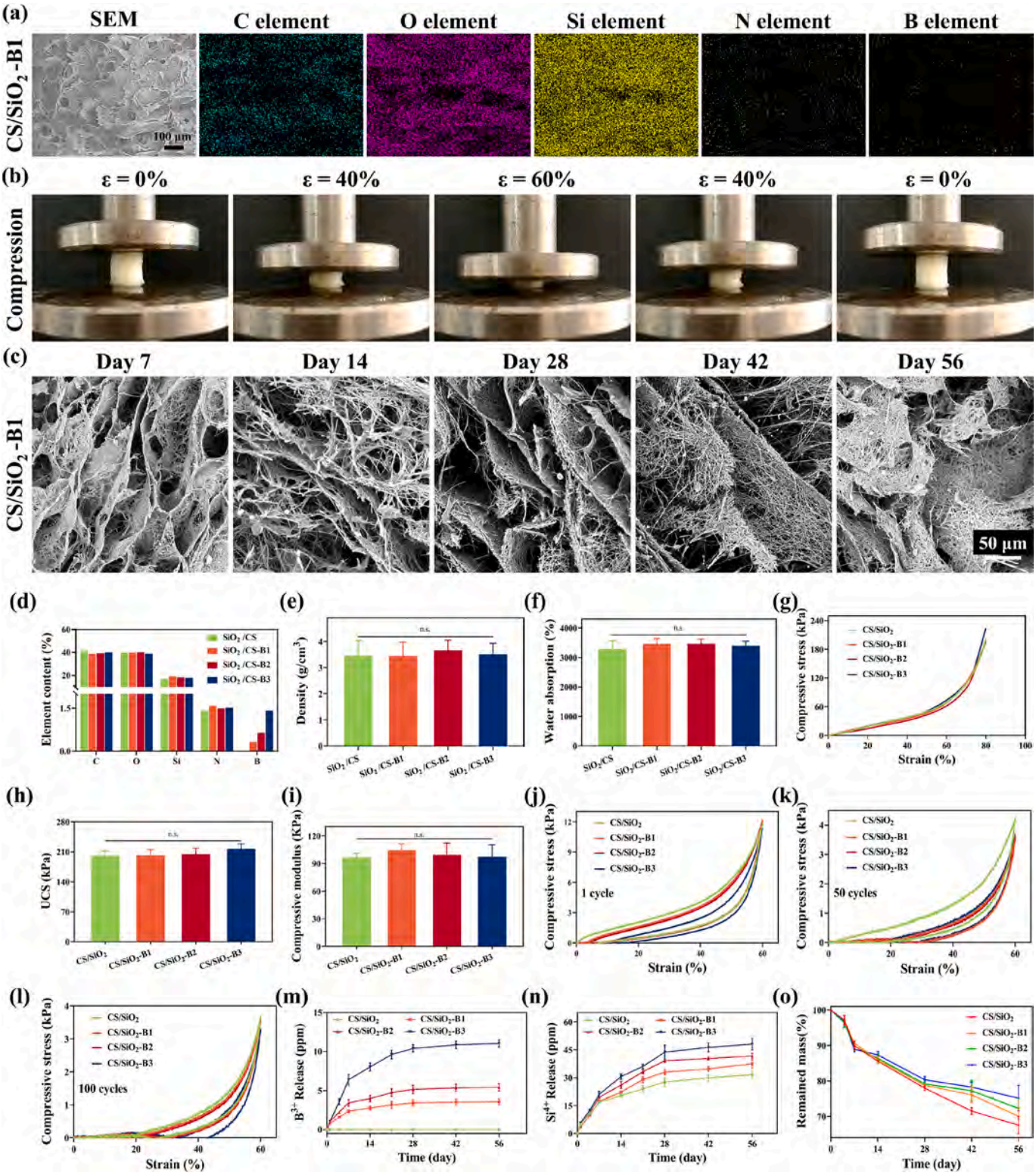

Fig. 3. Structural and morphological analysis of scaffolds as well as their mechanical properties. (a) SEM and EDS mapping images of CS/SiO_2-B1 scaffolds. Scale bar, 10 μm. (b) Macroscopic structural changes of CS/SiO_2-B1 scaffolds during a single compression and shape recovery process. (c) SEM images of CS/SiO_2-B1 scaffolds after a pre-determined number of days (e.g., 7, 14, 28, 42, 56, etc.) of *in vitro* degradation. Elemental composition (d), density (e), and water absorption capacity (f) of CS/SiO_2, CS/SiO_2-B1, CS/SiO_2-B2, and CS/SiO_2-B3 scaffolds. Representative stress-strain curves in compression testing of scaffolds (g), UCS (h) and compression modulus (i) of CS/SiO_2, CS/SiO_2-B1, CS/SiO_2-B2 and CS/SiO_2-B3 scaffolds in dry state under 80 % compressive strain. First compression cycle (j) 50^{th} cycle (k) and 100^{th} cycle (l) of different types of scaffolds in the wet state. Release kinetics of boron ions (B^{3+}) (m) and silicon ions (Si^{4+}) (n) from scaffolds. (o) Degradation curves of different scaffolds $^{*}P < 0.05$, $^{**}P < 0.01$, and $^{***}P < 0.001$.

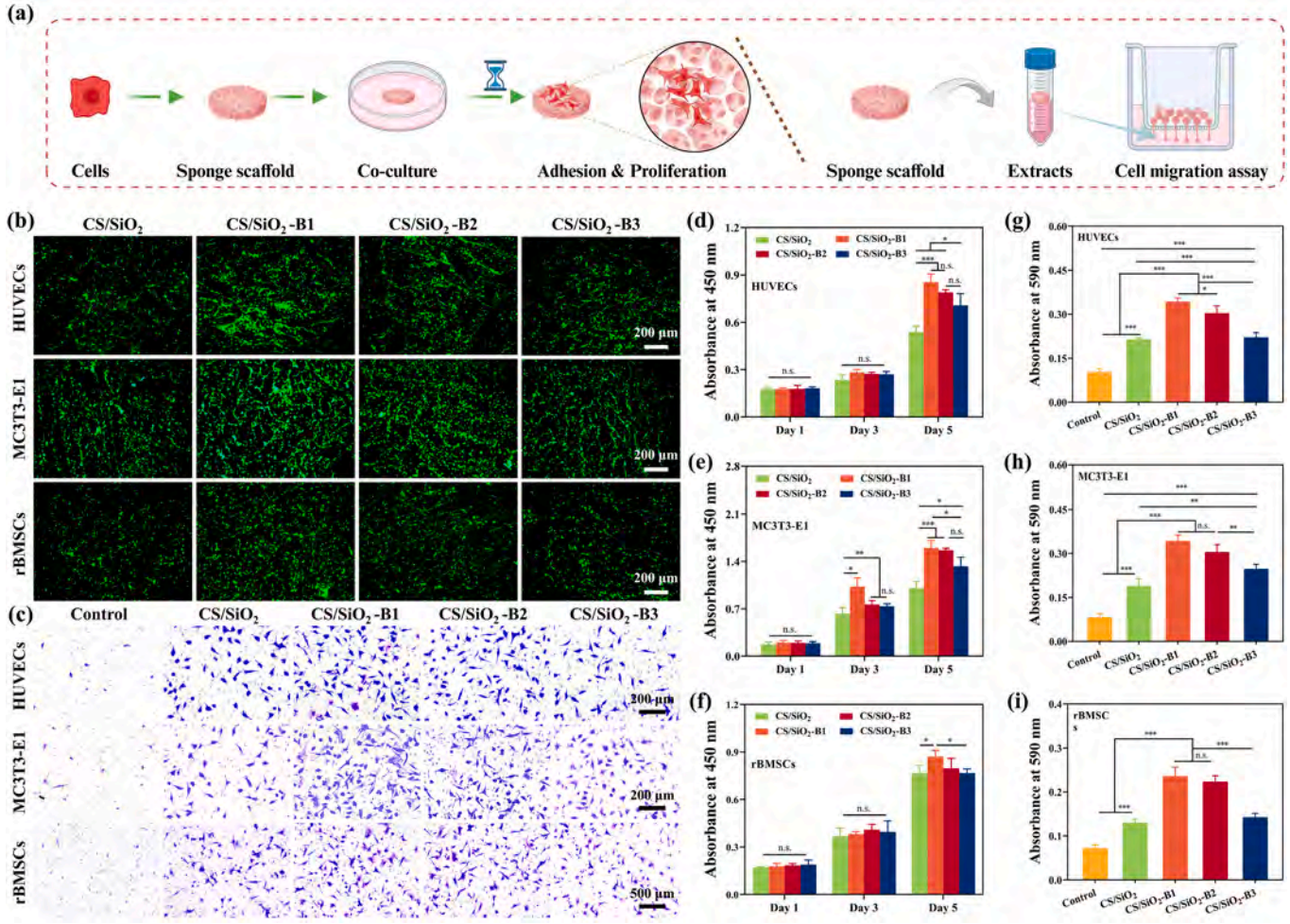

Fig. 4. Cytocompatibility of scaffolds *in vitro*. (a) Schematic illustration of cell proliferation on the sponge scaffolds and Transwell migration assay *in vitro*. (b) Live/dead staining of different cell types cultured on the scaffolds for up to day 5. Scale bar, 200 μm. (c) Representative images of transwell migration assay for HUVECs, MC3T3-E1, and rBMSCs at 12 h. Scale bar, 200 μm and 500 μm. (d-f) CCK-8 assay at day 1, 3, and 5 for HUVECs (d) MC3T3-E1 (e) and rBMSCs (f) seeded on the scaffolds. (g-i) Quantitative analysis of cell migration rate in transwell migration assays for HUVECs (g) MC3T3-E1 (h) and rBMSCs (i). *P < 0.05, **P < 0.01, and ***P < 0.001.

3.4. Osteogenic effects of sponge scaffolds

The osteogenic effects of scaffolds were evaluated using ALP and ARS staining *in vitro* (Fig. 6b). At day 7, CS/SiO_2, CS/SiO_2-B1, CS/SiO_2-B2, and CS/SiO_2-B3 scaffold groups exhibited higher ALP and ARS staining than that of the control group, while there was an insignificant difference among differnet types of scaffold groups. At day 14, CS/SiO_2-B1 group expressed the strongest purple staining in comparison to the other groups, which is indicative of the highest ALP activity (Fig. 6c). ARS staining further showed significantly higher biomineralization in CS/SiO_2-B1 scaffolds than that of the other scaffolds (Fig. 6d).

To explore the molecular mechanisms underlying scaffold-induced osteogenesis *in vitro*, qRT-PCR was performed and the expression of various osteogenesis-related genes in rBMSCs was assessed, such as OPN, OCN, COL-I, and RUNX2 (Fig. 6a). rBMSCs treated with CS/SiO_2, CS/SiO_2-B1, CS/SiO_2-B2, and CS/SiO_2-B3 scaffolds showed significantly higher mRNA expression levels of OPN, COL-I and OCN at both 7 days and 14 days compared to the control group. In contrast, the expression of RUNX2, which is involved in an earlier differentiation of osteoblasts was decreased at day 14 (Fig. 6e-h). Taken together, scaffolds containing boron exhibited significantly higher levels of osteogenic gene expression than that of the CS/SiO_2 scaffold. Among different types of boron-containing scaffolds, CS/SiO_2-B1 showed the highest gene expression levels. These results indicated that incorporation of silicon ions (Si^{4+}) and boron ions (B^{3+}) could upregulate the expression of osteogenic genes, and CS/SiO_2-B1 scaffolds possessed an optimal osteogenic function *in vitro*.

3.5. Antibacterial activity and hemostatic ability of sponge scaffolds

The antibacterial effects of CS has been reported in the previous research (Mohandas et al., 2018). The antibacterial activity of the scaffolds was determined against *E. coli* and *S. aureus*. Bacterial counts in each group were visually assessed on agar plates (Fig. 7a-b). The SiO_2 SF group exhibited negligible antibacterial effects (Cui et al., 2024). It has been reported that CS exhibits effective antibacterial effects against both bacterial strains. The survival rate of both types of bacteria on the scaffold groups was below 5 %, with no significant difference in antibacterial performance among the different scaffolds (Fig. 7e-f). We captured SEM images of bacteria after co-culturing with the scaffold to further investigate the antimicrobial effect of the scaffold. In the control group without co-culture, the morphology of *E. coli* and *S. aureus* remained in an original form, exhibiting intact rod-shaped and coccoid structures, respectively. After co-culture with the SF, no significant changes in bacterial morphology were observed, indicating that the antibacterial effect of the SiO_2 component was negligible. In contrast, after co-culture with the CS-containing scaffold, *E. coli* exhibited contraction alongside large number of folds on the bacterial surface.

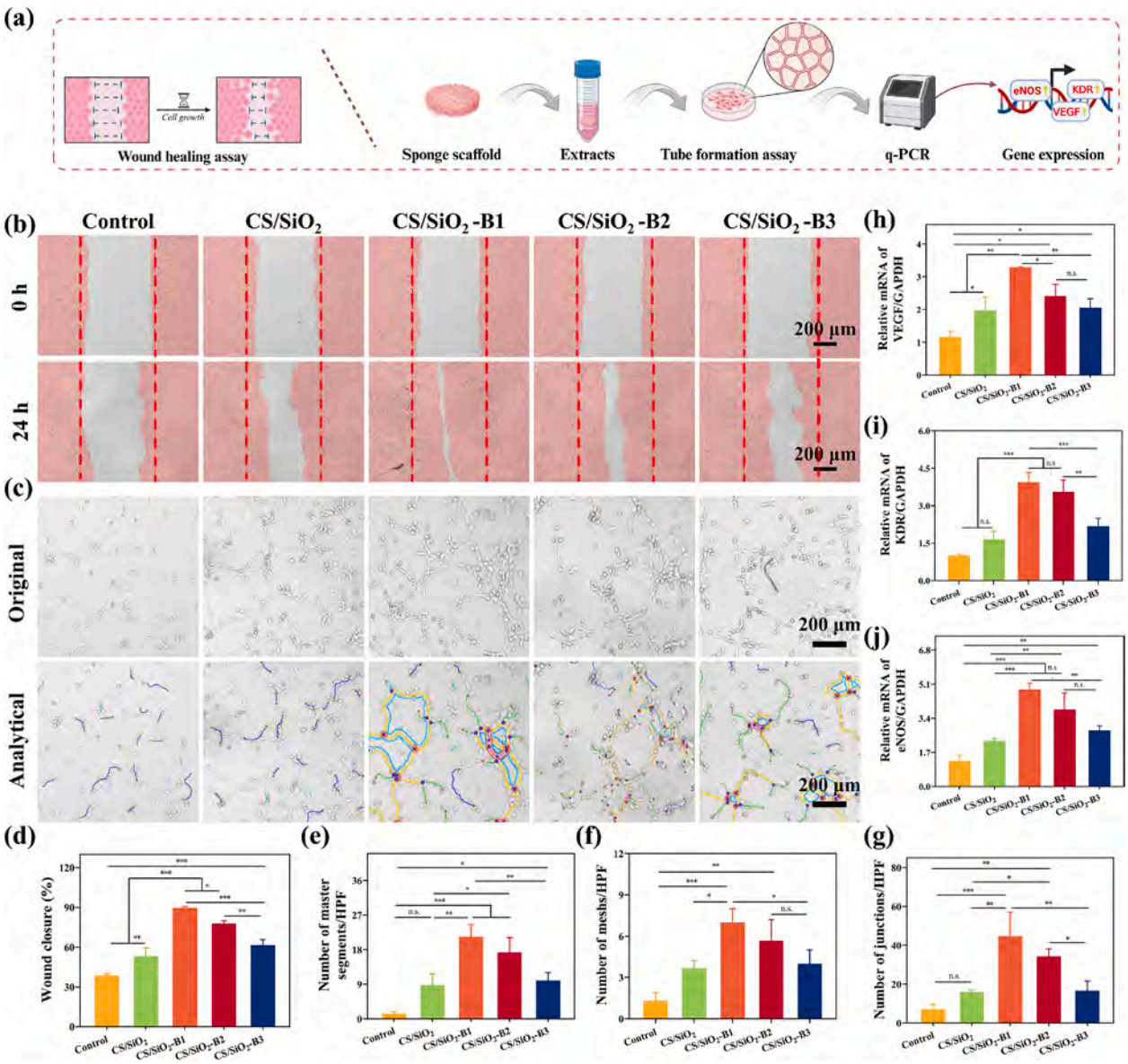

Fig. 5. Angiogenic effects of scaffolds *in vitro*. (a) Schematic illustration of wound healing assay, the process of tube formation assay and qRT-PCR analysis of angiogenesis-related genes in HUVECs cultured along with the extract solution of different types of sponge scaffolds. (b) Wound healing assay of HUVECs at 0 h and. Scale bar 200 μm. (c) Tubular network formation of HUVECs. In the analyzed images, dark blue dots represent nodes, red circles around the dark blue dots represent junctions, light blue circles represent meshes, yellow circles represent master segments, blue lines represent ends, and green lines represent branches. Scale bar, 200 μm. (d) Quantification of scratch healing rate. (e-g) Quantitative analysis of the structural parameters of the HUVEC tubular network, including the number of master segments (e), meshes (f) and junctions (g). (h-j) Expression of angiogenesis-related genes VEGF (f), KDR (g) and eNOS (h) in HUVECs after 5 days of culture with scaffold extract. $^{*}P < 0.05$, $^{**}P < 0.01$, and $^{***}P < 0.001$. (For interpretation of the references to colour in this figure legend, the reader is referred to the web version of this article.)

Similarly, *S. aureus* showed ruptures at the edges and bacterial shrinkage once co-cultured with the extract solution of CS-containing scaffolds. Since the incorporation of boron (B) did not significantly affect the antibacterial effect of the scaffold, antibacterial properties of the scaffold can be ascribed to the CS component (Supplementary Materials Fig. S8).

Rapid hemostasis at the site of bone injury is crucial for preventing hematoma formation in areas with unavoidable bone defects, which can hinder bone healing (Zhang et al., 2024). The *in vitro* coagulation function of the scaffolds was examined using blood coagulation index (BCI) (Fig. 7a). As compared to the control and SiO_2 FM groups, porous structure as well as CS may promote blood clot formation in sponge scaffolds (Fig. 7c). The BCI values for the control, SiO_2 FM, CS/SiO_2, CS/SiO_2-B1, CS/SiO_2-B2, and CS/SiO_2-B3 groups were 92.5 ± 3.1 %, 90.3 ± 4.2 %, 39.5 ± 1.2 %, 37.3 ± 0.6 %, 36.5 ± 1.3 %, and 36.1 ± 1.5 %, respectively (Fig. 7g).

Moreover, the hemocompatibility of the material is also an important indicator of its performance (Zhang et al., 2018). The hemolysis assay showed that solution of the positive control group was turned into dark red colour due to the rupture of red blood cells, while no significant colour change was observed in the negative control or any of the scaffold groups (Fig. 7d). Quantitative analysis indicated that the hemolysis rates for CS/SiO_2, CS/SiO_2-B1, CS/SiO_2-B2, and CS/SiO_2-B3 scaffolds were within the international standard range (≤5 %), indicating good hemocompatibility of all material groups (Fig. 7h).

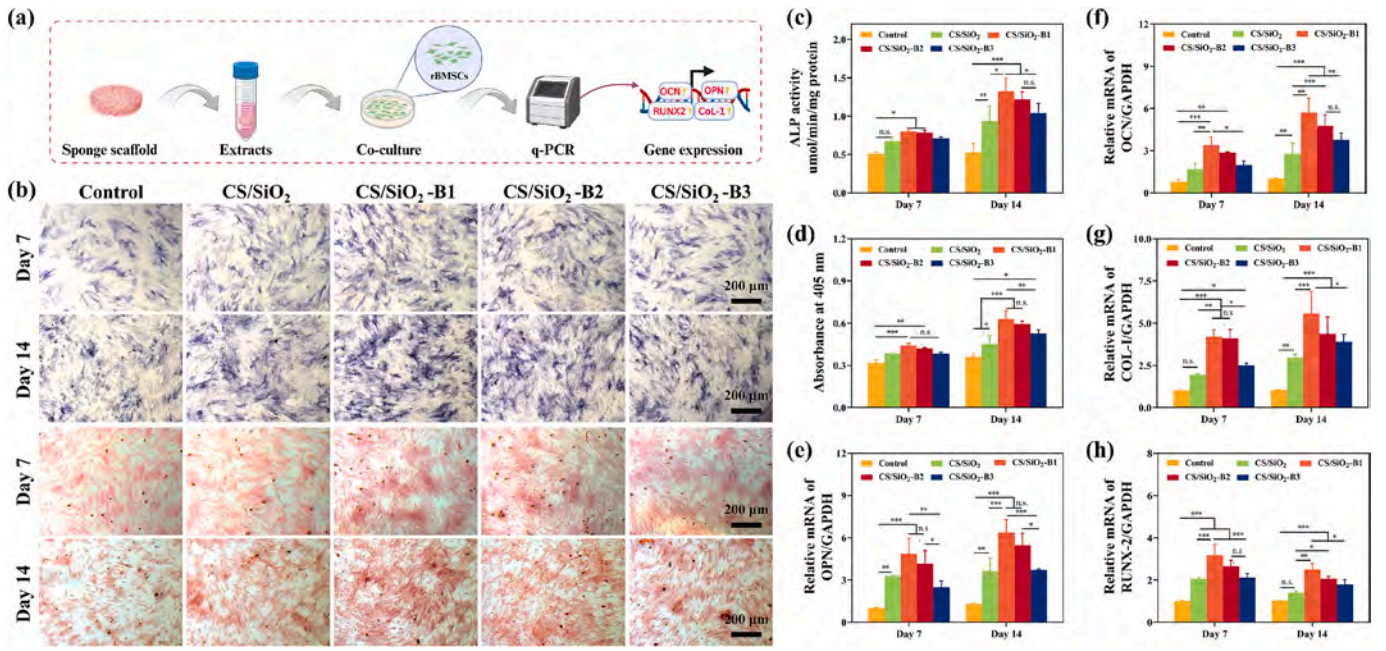

Fig. 6. Osteogenic ability of scaffolds *in vitro*. (a) Schematic diagram showing the procedure for evaluating the osteogenic effects of the extract solution of different types of scaffolds on rBMSCs and the analysis of osteogenesis-related genes by qRT-PCR. (b) ALP and ARS staining images of rBMSCs at day 7 and 14. Scale bar, 200 μm. ALP activity (c) and quantitative analysis of calcium deposition by ARS staining (d) in rBMSCs at day 7 and 14. (e-h) Expression of osteogenic-related genes OPN (e), OCN (f), COL-I (g), and RUNX2 (h) in rBMSCs cultured in osteogenic induction medium containing containing the extract solution of different types of scaffolds for up to 7 and 14 days. *P < 0.05, **P < 0.01, and ***P < 0.001.

3.6. Anti-inflammatory and antioxidant capacity of sponge scaffolds

Inflammatory response plays a pivotal role in bone defect repair by initiating the healing process. Macrophages, as one of the key cells involved in inflammation, can express different types of phenotypes, such as pro-inflammatory, M1 phenotype and an anti-inflammatory, M2 phenotype (Zhou et al., 2024). M1 macrophages promote inflammation, while M2 macrophages facilitate tissue repair and anti-inflammatory effects. The polarization of macrophages from M1 phenotype to the M2 phenotype is considered as a potential anti-inflammatory therapeutic approach (Fig. 8a). We additionally investigated the effects of sponge scaffolds on ROS clearance and macrophages polarization upon exposure to the LPS.

Flow cytometry was used to analyze the expression of the M1 phenotype ($CD86^+$) and M2 phenotype ($CD206^+$) of macrophages. Extract solution from sponge scaffolds showed higher proportion of $CD206^+$ M2 macrophages than that of the control group; CS/SiO_2-B1 group outperformed the other groups in terms of the proportion of $CD206^+$ M2 macrophages (5.70 %) (Fig. 8b). In the SF group, the M2/M1 ratio was similar to that of the control group, indicating that the effect of SiO_2 on macrophages polarization was negligible. The CS/SiO_2 group, which contained CS, exhibited slightly higher M2/M1 ratio than that of the control and SF groups, which is indicative of its anti-inflammatory effect of CS. The CS can promote macrophages polarization from the M1 phenotype toward M2 phenotype (Feng et al., 2021). When boron was added into the scaffolds, anti-inflammatory capability of sponge scaffold was increased. CS/SiO_2-B1 group exhibited significantly higher anti-inflammatory effect, which was also confirmed by quantitative flow cytometry data (Fig. 8d). It has indeed been previously shown that the boron ions (B^{3+}) can influence inflammatory response; low concentrations of boron ions (B^{3+}) can inhibit the expression of pro-inflammatory mediators (Bozkurt et al., 2022). Our study revealed a dose-dependent effect of boron ions (B^{3+}) on inflammation resolution, where higher concentrations of B^{3+} may suppress macrophage activity, which is also in consistence with the results from other *in vitro* experiments.

The ROS scavenging ability of macrophages was assessed using a ROS detection kit. CS/SiO_2-B1 exhibited significantly higher ROS scavenging ability and effectively suppressed oxidative stress in comparison to the control and other experimental groups (Fig. 8c). Quantitative results further showed significantly less percentage of ROS in the CS/SiO_2-B1 group than that of the other groups, which is also in agreement with the findings from fluorescence staining (Fig. 8e).

NO is a multifunctional signaling molecule, which plays a pivotal role in regulating the inflammatory response. We measured the NO content (μmol/well) in macrophages treated with the extract solution of different types of scaffolds to further evaluate anti-inflammatory effects of the scaffolds. The NO levels in the control group, CS group, and CS/SiO_2-B1 group were 6.6 ± 0.4, 5.6 ± 0.3, and 4.2 ± 0.2 μmol/well, respectively (Fig. 8f). These results showed that both CS and boron ions (B^{3+}) can reduce NO levels.

3.7. Animal experiments

In light of its optimal *in vitro* performance, CS/SiO_2-B1 was chosen for preliminary *in vivo* experiments. On the other hand, CS/SiO_2 was used as a control group to evaluate the beneficial effect of boron ions (B^{3+}) on bone tissue repair. CS/SiO_2 and CS/SiO_2-B1 scaffolds were implanted in a rat calvarial defect model (Fig. 9). Micro-CT imaging of the defect site at 3 and 6 weeks post-implantation demonstrated osteogenic ability of boron-loaded scaffolds (Fig. 9b). At 3 weeks, the control group showed minimal bone formation within the defect area (red circles represent the original defect area). On the other hand, boron-loaded scaffolds exhibited significantly higher mineralization at the defect site.

At 6 weeks, the control group displayed a small amount of new bone formation in the central region, with the mineralized tissue expanding inward. In contrast, the CS/SiO_2 group showed a marked increase in the new bone coverage, while the boron-doped CS/SiO_2-B1 group manifested more pronounced mineralization. Quantitative analysis revealed that the BV/TV of the CS/SiO_2-B1 group (20.8 ± 0.9 %) was significantly higher than that of the CS/SiO_2 group (17.4 ± 1.5 %) at 6 weeks pot-implantation (Fig. 9c). Moreover, the bone density of the CS/SiO_2-

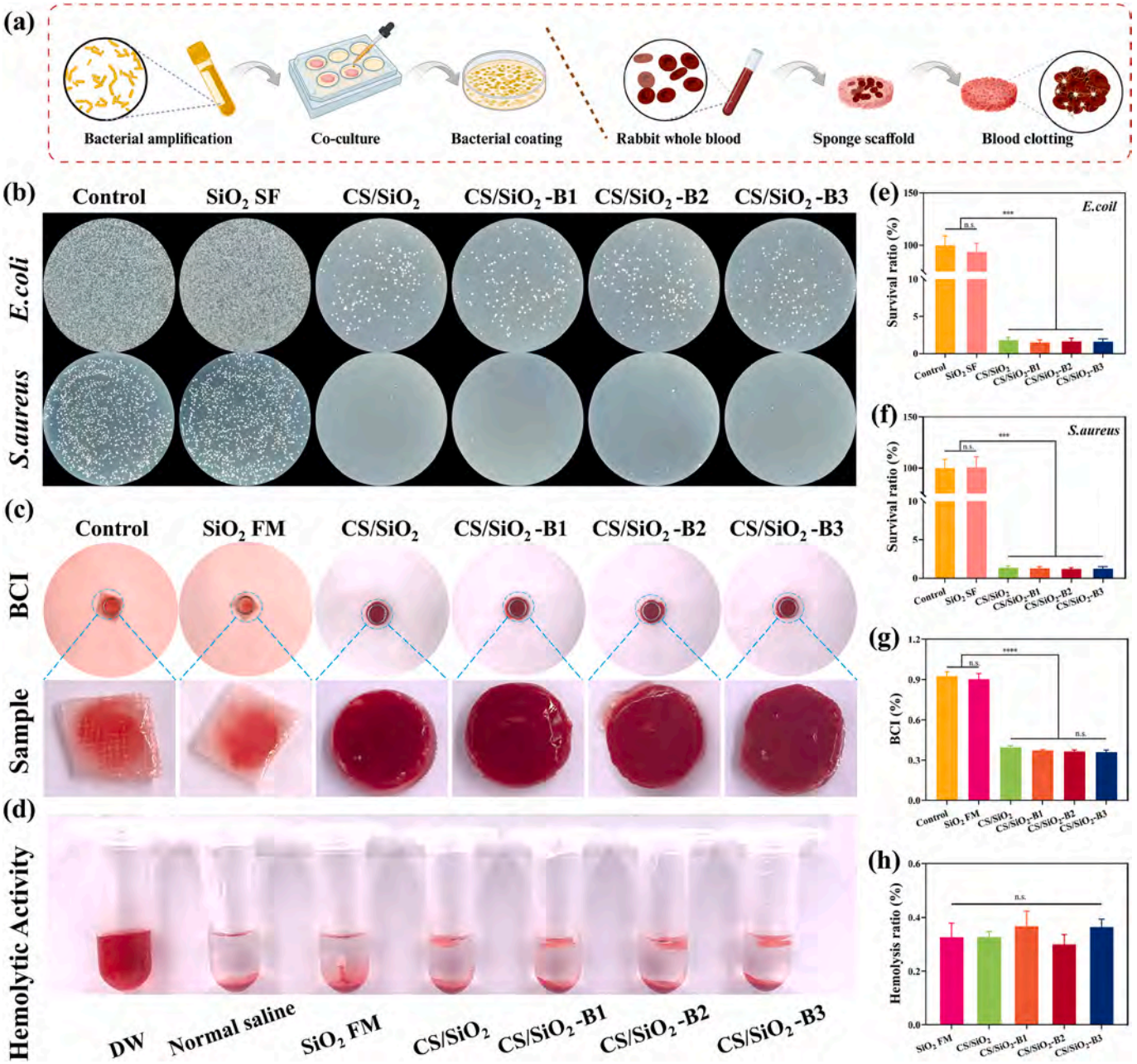

Fig. 7. Antibacterial activity and hemostasis assays of sponge scaffolds *in vitro*. (a) Schematic illustration of antibacterial test and blood clotting of scaffolds. (b) Macroscopic images of *E. coli* and *S. aureus* grown on agar plates after co-culture with the scaffold. (c) Macroscopic images of blood clots in a dynamic whole blood coagulation model of SiO_2 FM and four types of scaffolds. (d) Macrophotograph of hemolysis tests of SiO_2 FM and different scaffolds. Survival rates of *E. coli* (e) and *S. aureus* (f) treated with different types of scaffolds. Blood coagulation index (BCI) values (g) and hemolysis rate (h). $^{*}P < 0.05$, $^{**}P < 0.01$, and $^{***}P < 0.001$.

B1 group (0.315 ± 0.037 g/cm^3) was significantly higher than that of the CS/SiO_2 group (0.230 ± 0.032 g/cm^3) (Fig. 9d). H&E and Masson's trichrome staining were used to determine extent of new bone formation and tissue integration at the defect site (Fig. 9e-f). A large amount of cell infiltration was observed within the scaffold, while only a limited bone/osteoid formation was observed in the control group. Whereas, the CS/SiO_2 and the CS/SiO_2-B1 scaffolds promoted more new bone formation (indicated by the red dashed box). Particularly, CS/SiO_2-B1 scaffolds enhanced matrix mineralization and promoted the formation of mature bone clusters at the bottom of the defect site. In addition, immunohistochemical staining was performed for osteogenic markers, such as OCN and OPN. The OCN is secreted by differentiated and mature osteoblasts and deposited in the bone matrix, primarily appearing during the mineralization phase. On the other hand, OPN is secreted by osteoblasts, osteocytes, and other cells, which can be observed in the cytoplasm of osteoblasts and osteocytes. The staining results showed that both OCN and OPN expression in the CS/SiO_2-B1 scaffold group were higher than in the other groups, which is consistent with the results from H&E and Masson staining (Supplementary Materials Fig. S9). Although, CS/SiO_2-B1 scaffolds demonstrated the best osteogenic performance *in vivo*, overall bone regeneration effect was limited, which can be ascribed to the large volume of the implanted scaffold and its slow degradation rate.

4. Discussion

Bone defects are currently treated using different types of materials, among which BG is one of the most commonly used candidature. BG is a biocompatible material, which can bind with bone and stimulate bone

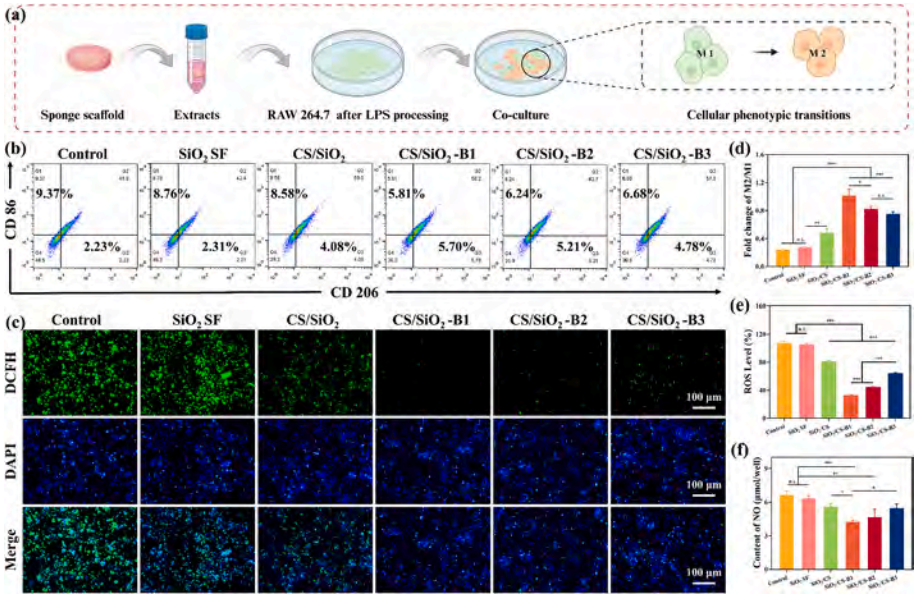

Fig. 8. Anti-inflammatory and anti-oxidative capacity of sponge scaffolds *in vitro*. (a) Schematic illustration of macrophages polarization from pro-inflammatory phenotype (M1) to anti-inflammatory phenotype (M2) induced by the extract solution of different types of scaffolds *in vitro*. (b) Flow cytometry analysis showing an influence of different type of scaffolds on cell phenotype. (c) Fluorescence staining images of ROS scavenging effect of different types of scaffolds. Quantitative analysis of the fold change of M2/M1(d), ROS scavenging effect (e) and quantitative analysis of the NO production (f). D. $^{*}P < 0.05$, $^{**}P < 0.01$, and $^{***}P < 0.001$.

regeneration by releasing therapeutic ions that can promote cellular responses and tissue growth. However, BG is relatively brittle and is prone to fracture under mechanical loads (Granel et al., 2019). In addition, BG is often prepared in bulk, granular, or foam forms, which do not closely mimic the structure of bone (El-Rashidy et al., 2017). By fabricating BG into flexible nanofibers and further transforming it into sponges, the BG can achieve lightweight characteristics, high porosity, and an excellent biocompatibility. These BG-loaded scaffolds can promote cell growth and bone tissue regeneration. In this study, we incorporated trace amounts of boron into a silica network to synthesize flexible SiO_2-B_2O_3 (SiO_2-B) nanofiber membranes. Flexible boron-doped SiO_2 nanofibers were homogenized into SF and were combined with CS to form a 3D porous scaffold. The addition of a small amount of GA enabled chemical cross-linking, resulting in the encapsulation and bonding of the SF within the CS matrix (Fig. 1a). This approach may not only overcome the brittleness of BG fibers but it may also allow for an independent investigation of the effects of varying boron ion concentrations on both *in vitro* and *in vivo* biological behaviors.

To realize ECM-mimetic scaffolds that closely resemble the ratio of inorganic/organic component, homogenized flexible membrane was mixed with CS at a ratio of 65:35 to prepare the CS/SiO_2-B sponge scaffolds (Liu et al., 2023). Previous studies have reported the preparation of flexible SiO_2, aluminum oxide (Al_2O_3), and zirconium dioxide (ZrO_2) nanofibers by adjusting the composition of spinning solution, electrospinning parameters, and calcination temperature (Mao et al., 2016; Zhao et al., 2011; Zhu et al., 2024). Boron typically forms a boron-silicon network and can be combined with the other metal oxides, such as sodium oxide (Na_2O), potassium oxide (K_2O), calcium oxide (CaO), and phosphorus pentoxide (P_2O_5), to create borosilicate bioactive glass (BSG) (Liu et al., 2024). The synthesized BSG is usually in powder form and releases various ions that can synergistically act to promote bone tissue repair. However, to the best of the authors' knowledge, only a handful of studies have investigated the biological role of boron in the BSG preparation.

The fabrication of sponges from SiO_2-B1 short nanofibers and CS endowed the nanofibers with an excellent porous structure (Fig. 2e). This structure showed significantly higher water uptake, which may have implications for tissue repair (Fig. 3f). As compared to two-dimensional (2D) membranes, 3D structure mimicking the ECM, can provide a favorable environment for cell adhesion and proliferation. The interconnected porous structure of scaffolds can furnish more active sites for ion interactions and release, thereby promoting the transport of boron ions (B^{3+}) and silicon ions (Si^{4+}) (Fig. 3m-n) (Balasubramanian et al., 2016).

The hydrophilicity of implanted materials plays a crucial role in facilitating the transport of nutrients and waste products, which is crucial for cellular metabolism and tissue health (Wei et al., 2024). Moreover, elastic mechanical properties of scaffolds are essential for mimicking the natural flexibility of bone tissue (Jakus et al., 2016). In its hydrated state, CS possesses high elasticity and flexibility, which allows it to quickly return to its original shape after compression (Li et al., 2018). This property may be particularly advantageous for conforming to the morphology of bone defects and providing continuous mechanical support during the healing process. The incorporation of nanofibers into CS further enhanced the compressive stress of scaffolds. The CS/SiO_2-B sponge scaffolds maintained their original shape even after 100 compression cycles (Fig. 3j-l). Such high elasticity may allow the scaffold to better integrate with the surrounding bone tissue, thereby helping to absorb mechanical loads, reduce stress concentration, and prevent scaffold fracture (Wang, Zhou, et al., 2024, Gholap et al., 2024). Additionally, the flexible structure of the scaffold may leverage a conducive mechanical environment to dynamically adapt to the defect site, thereby promoting cell adhesion, proliferation, and differentiation (Saravanan et al., 2016).

In the CS/SiO_2-B scaffold, the inorganic components are primarily composed of silica (SiO_2) and small amounts of boron. SiO_2 has been widely used to promote tissue repair. Wang et al. fabricated SiO_2-based sponges for skin tissue repair (Wang, Zhou, et al., 2024). Release of silicon ions (Si^{4+}) and calcium ions (Ca^{2+}) ions from the scaffold displayed excellent hemostatic properties and promoted rapid wound healing. Similarly, boron has been shown to enhance cellular activity and mineralization, thereby supporting bone growth and healing (Hakki et al., 2010).

The improved angiogenesis can be ascribed to the pro-angiogenic effects of silicon ions (Si^{4+}) and boron ions (B^{3+}). Silicon ions (Si^{4+}) enter the cells through ion transport proteins, while boron ions (B^{3+}) are transported into the cells *via* the borate transporter (Liao et al., 2010). Both ions accelerate VEGF production *via* RAS/MAPK signaling

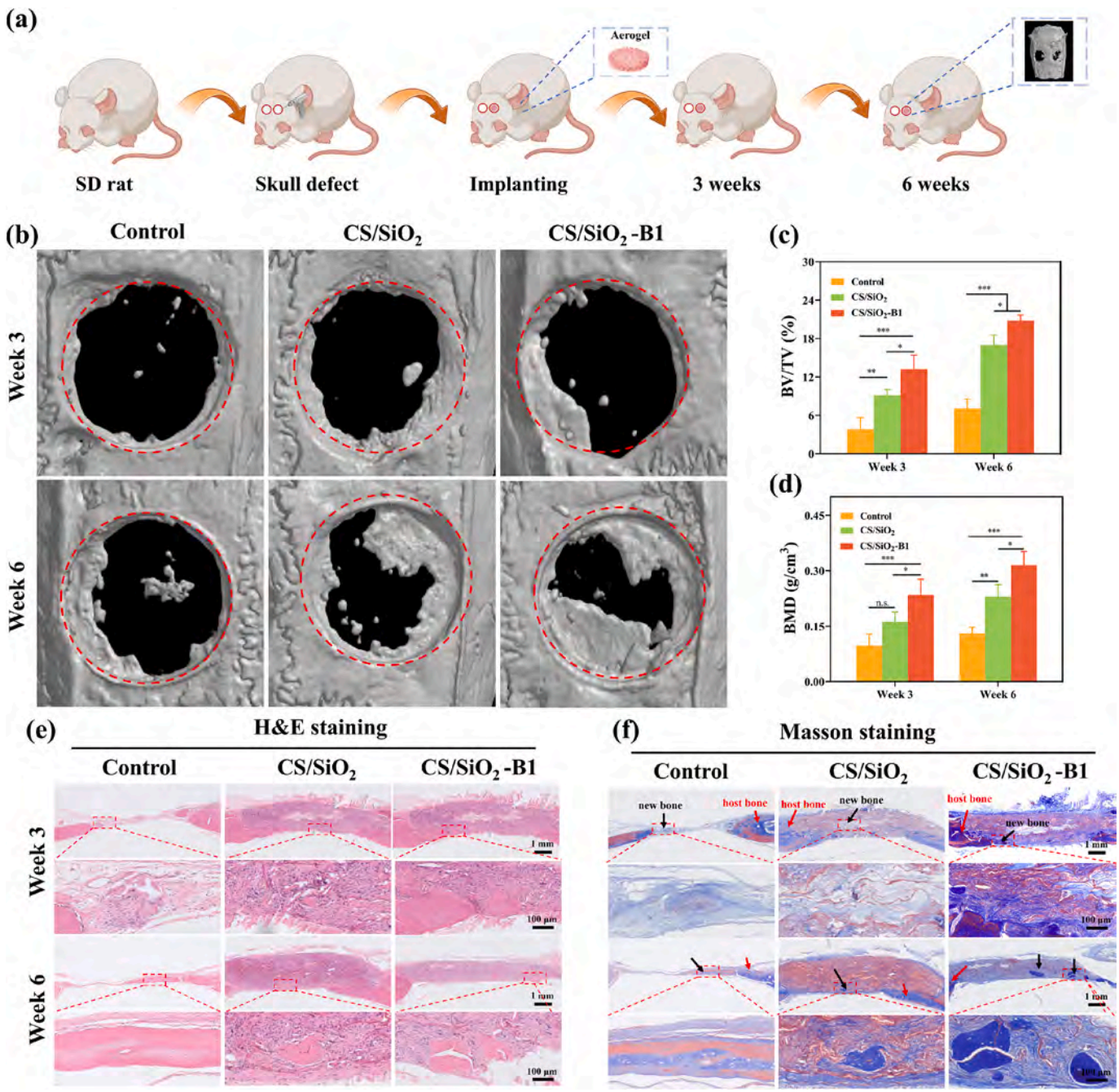

Fig. 9. Osteogenic ability of scaffolds *in vivo*. (a) Schematic illustration showing the preparation of a rat cranial defect model and *in vivo* implantation of the sponge scaffolds. (b) Micro-CT images of the rat cranial defect model at 3 and 6 weeks post-implantation of CS/SiO_2 and CS/SiO_2-B1 scaffolds. (c-d) Quantification of new bone volume fraction (BV/TV) and bone mineral density (BMD) at the cranial defect site. H&E staining (e) and MT staining (f) were used to observe the histological changes in new bone formation in the bone defect area after treatment with various scaffolds. *P < 0.05, **P < 0.01, and ***P < 0.001.

pathway, which subsequently activates angiogenesis signal cascade. This may have enhanced the expression levels of angiogenic genes, including VEGF, KDR, and eNOS (Fig. 5h-j). Boron can stimulate the secretion of pro-angiogenic factors, which may include upstream activation of the Phosphatidylinositol-3-kinase/Protein kinase B (PI3K/AKT) signaling pathway and downstream stimulation of VEGF/VEGFR2 in HUVECs (Li et al., 2019). Simultaneously, silicon can stimulate angiogenic pathways by increasing the expression of pro-angiogenic factors such as VEGF, FGF, and their receptors in HUVECs.

Flexible bioactive ceramic fibers can form a calcium phosphate (CaP)-enriched hydroxyapatite layer upon contact with body fluids, thereby resembling the inorganic components of natural bone (Kajander et al., 2023). These components, especially silicon ions (Si^{4+}) and boron ions (B^{3+}), not only support the proliferation of osteocytes but also guide the differentiation of rBMSCs toward osteoblasts, thereby accelerating bone regeneration. The rate of osteogenic differentiation is critical for bone injury repair (Qi et al., 2024). Studies have shown that both boron and silicon ions can induce osteogenic differentiation. Boron ions (B^{3+}) traverse through the cell membrane, they activate Wnt/β-catenin signaling pathway, particularly by enhancing the role of β-catenin in the nucleus, thus stimulating the expression of genes associated with osteogenesis and angiogenesis. In addition, boron ions (B^{3+}) can inhibit the receptor activator of nuclear factor-κB ligand (RANKL) signaling pathway, reducing osteoclast activity, decreasing bone resorption, and

promoting bone repair (Yin et al., 2018). On the other hand, silicon ions (Si^{4+}) stimulate bone formation by activating the PI3K/AKT signaling pathway (Kong et al., 2022).

In the early stages of bone injury, significant blood loss occurs (Yuan et al., 2024). Effective hemostasis can maintain the local blood supply and promote hematoma formation, which provides essential nutrients and cells necessary for bone healing (Xie et al., 2021). Therefore, the coagulation function of the material is pertinent for bone injury repair. The CS/SiO_2-B scaffolds demonstrated substantial *in vitro* hemostatic properties, which could facilitate rapid hemostasis upon implantation at bone defect sites (Fig. 7c). The positively charged CS molecular chains can attract the negatively charged cell wall and promote cell adhesion. The interaction between CS and RNCs results in cell aggregation and subsequent blood coagulation. Beside hemostatic function of the organic components, the porous structure of the CS/SiO_2-B scaffolds can provide a larger surface area for platelet adhesion and aggregation (2012, Ren et al., 2023). Furthermore, the ability of scaffolds to absorb more water supports them to absorb blood like a sponge, forming a physical barrier that prevents blood flow and facilitates localized hemostasis (Su et al., 2023).

The CS endows the scaffolds with an excellent antibacterial property. The surface of bacterial cell membrane is rich in anionic charges. In an acidic environment, the positively charged amino (NH_2) groups within the long chains of CS can be absorbed onto the surface of bacterial cell membrane through electrostatic interactions, thereby disrupting membrane permeability and inducing bacterial death. Besides, CS can penetrate bacterial cell wall and directly affect intracellular substances by interfering with bacterial DNA transcription and protein synthesis, which leads to the inhibition of bacterial metabolic activities (Li et al., 2011). CS can also bind to intracellular metal ions through chelation and disrupt bacterial enzymes and metabolic function (Lin et al., 2014; Rong et al., 2007; Wang et al., 2011). Despite chemical cross-linking of GA consumes some amino groups in CS, it has little effect on the antibacterial performance of CS/SiO_2-B scaffolds. Moreover, boron ions (B^{3+}) have been shown to inhibit bacterial activity (Zheng et al., 2024). However, the antibacterial performance of scaffolds with varying boron content did not show significant differences, presumably due to relatively low concentration of boron in the scaffolds. Overall, the antibacterial action of the scaffolds is primarily ascribed to CS.

The CS/SiO_2-B sponge scaffold, composed of CS and boron ions (B^{3+}), exhibits anti-inflammatory properties, which influence macrophages polarization, promoting macrophages polarization from pro-inflammatory M1 phenotype to anti-inflammatory M2 phenotype (Bozkurt et al., 2022; Xu et al., 2024). Additionally, the incorporation of low concentrations of boron ions (B^{3+}) further improve the ability of the scaffold to induce macrophages polarization toward the M2 phenotype (Fig. 8b). Oxidative stress is a key factor in inflammation, and antioxidant properties of scaffolds can help suppress ROS, thereby mitigating oxidative damage associated with inflammation (Fig. 8c).Moreover, NO, a molecule involved in the inflammatory process can promote inflammation, especially at higher levels of NO. CS and boron ions (B^{3+}) can suppress inflammation by reducing NO production (Fig. 8f).

Boron-doped SiO_2/CS elastic 3D sponge scaffold have shown significant osteogenic potential; the addition of boron further improved the osteogenic ability of scaffolds. Moreover, both *in vitro* and *in vivo* experiments showed that lower boron concentrations exhibit good biocompatibility and biological functionality. The degradation rate of sponge scaffolds *in vivo* is relatively low, and they can induce a certain degree of inflammation, which may limit the ability of the scaffolds to promote bone repair.

This study has also some limitations. For *in vivo* experiments, we did not compare the sponge scaffold with commercially available bone regeneration scaffolds, which may preclude comprehensive understanding of the ability of scaffolds to promote bone tissue repair. Moreover, scaffolds exhibited inferior mechanical properties than that of the bone tissues, which warrant further investigations to improve mechanical properties of scaffolds to further broaden their potential for the osteochondral tissue repair. Nevertheless, these boron-doped SiO_2/CS scaffolds manifested multifunctional characteristics, such as angiogenic effect, anti-bacterial properties, anti-inflammatory potential, release of therapeutic ions, and osteogenic ability, which may have broad implications for the bone tissue repair and potentially other bio-related disciplines.

5. Conclusion

In summary, we successfully prepared SiO_2-B FM scaffolds using sol-gel electrospinning method, followed by the homogenization of scaffolds into SF, and the blending of SF with CS to obtain ECM-mimicking sponge scaffolds. Boron-doped SiO_2/CS scaffolds demonstrated good elasticity in wet state. The porous structure of the scaffolds improved mechanical properties and promoted cell adhesion and proliferation. The incorporation of CS conferred antibacterial properties to the scaffolds by effectively inhibiting the proliferation of both Gram-positive and Gram-negative bacteria. Moreover, the CS/SiO_2-B1 scaffolds induced significant bone regeneration and ECM deposition in a rat cranial bone defect model. Taken together, these sponge scaffolds promoted effective bone tissue repair and warrant future investigation into their applicability in regenerative medicine.

CRediT authorship contribution statement

Zheng Lei: Writing – review & editing, Writing – original draft, Methodology, Investigation, Formal analysis. **Chunchun Li:** Software, Methodology. **Zhengchao Yuan:** Writing – review & editing, Software, Resources, Methodology. **Xinyi Wang:** Supervision, Methodology. **Guangfang Cai:** Visualization, Supervision, Software. **Panpan Shang:** Writing – review & editing, Visualization, Software, Resources. **Yue Zhao:** Visualization, Validation, Software, Resources. **Muhammad Rafique:** Writing – review & editing, Visualization, Methodology. **Mohamed EL-Newehy:** Visualization, Software, Funding acquisition. **Meera Moydeen Adulhameed:** Visualization, Software, Resources, Funding acquisition. **Muhammad Shafiq:** Writing – review & editing, Writing – original draft, Validation, Methodology. **Liang Song:** Visualization, Validation, Supervision, Software. **Hao Zheng:** Funding acquisition, Supervision. **Xiumei Mo:** Writing – review & editing, Writing – original draft, Visualization, Validation, Supervision, Resources, Project administration, Funding acquisition.

Declaration of competing interest

The authors declare that they have no known competing financial interests or personal relationships that could have appeared to influence the work reported in this paper.

Acknowledgments

This project was supported by Science and Technology Commission of Shanghai Municipality, China (20DZ2254900), Sino German Science Foundation Research Exchange Center, China (M-0263), Chenguang Program of Shanghai Education Development Foundation and Shanghai Municipal Education Commission (23CGB08), Natural Science Research Funds of Minhang District, Shanghai (2023MHZ015), Excellent Talent Project of Shanghai Fifth People's Hospital (2024WYRCZY01) and Shanghai Municipal Education Commission (23CGB08), and China Education Association for International Exchange (2022181). This project was also supported by Researchers Supporting Project Number (RSP2025R65), King Saud University, Riyadh, Saudi Arabia. Thanks to http://www.home-for-researchers.com for creating the Fig. 1.

Appendix A. Supplementary data

Supplementary data to this article can be found online at https://doi.org/10.1016/j.carbpol.2025.123491.

Data availability

Data will be made available on request.

References

Afshar, H. A., & Ghaee, A. (2016). Preparation of aminated chitosan/alginate scaffold containing halloysite nanotubes with improved cell attachment. *Carbohydrate Polymers, 151*, 1120–1131.

Balasubramanian, P., Hupa, L., Jokic, B., Detsch, R., Grünewald, A., & Boccaccini, A. R. (2016). Angiogenic potential of boron-containing bioactive glasses: In vitro study. *Journal of Materials Science, 52*, 8785–8792.

Barbosa, F., Garrudo, F. F. F., Alberte, P. S., Resina, L., Carvalho, M. S., Jain, A., … Silva, J. C. (2023). Hydroxyapatite-filled osteoinductive and piezoelectric nanofibers for bone tissue engineering. *Science and Technology of Advanced Materials, 24*, Article 2242242.

Bozkurt, S. B., Nielsen, F. H., & Hakki, S. S. (2022). Boric acid reverses nicotine-induced cytokine expressions of human gingival fibroblasts. *Biological Trace Element Research, 201*, 1174–1180.

Brown, R. F., Rahaman, M. N., Dwilewicz, A. B., Huang, W., Day, D. E., Li, Y., & Bal, B. S. (2008). Effect of borate glass composition on its conversion to hydroxyapatite and on the proliferation of MC3T3-E1 cells. *Journal of Biomedical Materials Research Part A, 88A*, 392–400.

Cai, P., Cao, L., Ding, Y., Han, Y., Yu, X., Cui, J., … Sun, B. (2024). Modified highly elastic 3D nanofiber embolic scaffolds for precise in situ embolization therapy. *Advanced Functional Materials, 34*, Article 2316590.

Chen, F., Song, Z., Gao, L., Hong, H., & Liu, C. (2016). Hierarchically macroporous/mesoporous POC composite scaffolds with IBU-loaded hollow SiO_2 microspheres for repairing infected bone defects. *Journal of Materials Chemistry B, 4*, 4198–4205.

Chen, Z., Zheng, J., Pei, X., Sun, S., Cai, J., Liu, Y., Wang, Y., Zheng, L., & Zhou, H. (2023). Ultrasound-driven electrical stimulation based on 3D hierarchical porous piezoelectric nanofiber-aerogel scaffold promotes bone defect repair. *Chemical Engineering Journal, 470*, Article 144305.

Cheng, G., Xie, C., Cheng, Y., Gong, C., Li, Z., Dong, X., Deng, H., & Li, Z. (2022). Enhanced mineralization of the nanofibers-incorporated aerogels increases mechanical properties of scaffold and promotes bone formation. *Materials Today Advances, 16*, Article 100318.

Cui, J., Cai, Y., Yu, X., Shen, Y., Zhou, T., Sun, B., … Mo, X. (2024). Flexible copper-doped silica fibers promote infected conjunctival tissue repair through antibacterial and anti-inflammatory effects. *Advanced Fiber Materials, 6*, 278–296.

Donoiu, I., Militaru, C., Obleagă, O., Hunter, J. M., Neamţu, J., Biţă, A., … Rogoveanu, O. C. (2018). Effects of boron-containing compounds on cardiovascular disease risk factors – A review. *Journal of Trace Elements in Medicine and Biology, 50*, 47–56.

El-Rashidy, A. A., Roether, J. A., Harhaus, L., Kneser, U., & Boccaccini, A. R. (2017). Regenerating bone with bioactive glass scaffolds: A review of *in vivo* studies in bone defect models. *Acta Biomaterialia, 62*, 1–28.

Feng, Y., Gao, H. L., Wu, D., Weng, Y. T., Wang, Z. Y., Yu, S. H., & Wang, Z. (2021). Biomimetic lamellar chitosan scaffold for soft gingival tissue regeneration. *Advanced Functional Materials, 31*, Article 2105348.

Gholap, A. D., Rojekar, S., Kapare, H. S., Vishwakarma, N., Raikwar, S., Garkal, A., … Annapure, U. (2024). Chitosan scaffolds: Expanding horizons in biomedical applications. *Carbohydrate Polymers, 323*, Article 121394.

Granel, H., Bossard, C., Nucke, L., Wauquier, F., Rochefort, G. Y., Guicheux, J., … Wittrant, Y. (2019). Optimized bioactive glass: The quest for the bony graft. *Advanced Healthcare Materials, 8*, Article 1801542.

Hakki, S. S., Bozkurt, B. S., & Hakki, E. E. (2010). Boron regulates mineralized tissue-associated proteins in osteoblasts (MC3T3-E1). *Journal of Trace Elements in Medicine and Biology, 24*, 243–250.

Huang, C., Shi, S., Qin, M., Rong, X., Ding, Z., Fu, X., … Zhou, Z. (2024). A composite hydrogel functionalized by borosilicate bioactive glasses and VEGF for critical-size bone regeneration. *Advanced Science, 11*, Article 2400349.

Jakus, A. E., Rutz, A. L., Jordan, S. W., Kannan, A., Mitchell, S. M., Yun, C., … Shah, R. N. (2016). Hyperelastic "bone": A highly versatile, growth factor-free, osteoregenerative, scalable, and surgically friendly biomaterial. *Science Translational Medicine, 8*, Article 358ra127.

Kajander, K., Sirkia, S. V., Vallittu, P. K., Heino, T. J., & Maatta, J. A. (2023). Bioactive glasses promote rapid pre-osteoblastic cell migration in contrast to hydroxyapatite, while carbonated apatite shows migration inhibiting properties. *Scientific Reports, 13*, 20587.

Ke, C.-L., Deng, F.-S., Chuang, C.-Y., & Lin, C.-H. (2021). Antimicrobial actions and applications of chitosan. *Polymers, 13*, 904.

Kong, Y., Zhang, X., Ma, X., Wu, L., Chen, D., Su, B., Liu, D., & Wang, X. (2022). Silicon-substituted calcium phosphate promotes osteogenic-angiogenic coupling by activating the TLR4/PI3K/AKT signaling axis. *Journal of Biomaterials Applications, 37*, 459–473.

Li, K., Lu, X., Razanau, I., Wu, X., Hu, T., Liu, S., Xie, Y., Huang, L., & Zheng, X. (2019). The enhanced angiogenic responses to ionic dissolution products from a boron-incorporated calcium silicate coating. *Materials Science and Engineering: C, 101*, 513–520.

Li, M., Xu, T., & Xin, M. (2011). Research progress of antibacterial activity of chitosan and its derivatives. *Chemical Industry and Engineering Progress, 30*, 203–209.

Li, P., Jia, Z., Wang, Q., Tang, P., Wang, M., Wang, K., Fang, J., Zhao, C., Ren, F., Ge, X., & Lu, X. (2018). A resilient and flexible chitosan/silk cryogel incorporated Ag/Sr co-doped nanoscale hydroxyapatite for osteoinductivity and antibacterial properties. *Journal of Materials Chemistry B, 6*, 7427–7438.

Liao, S. F., Monegue, J. S., Lindemann, M. D., Cromwell, G. L., & Matthews, J. C. (2010). Dietary supplementation of boron differentially alters expression of borate transporter (NaBCl) mRNA by jejunum and kidney of growing pigs. *Biological Trace Element Research, 143*, 901–912.

Lin, S., Li, M., Xin, M., & Wang, C. (2014). Progress in antimicrobial mechanism of chitosan and its derivatives. *Chemistry, 77*, 220–226.

Liu, C., Wang, X., Shu, D., Li, S., Zhnag, L., Cui, X., … Pan, H. (2024). Progress on promoting wound healing with boric acid/borosilicate bioactive glass. *Journal of the Chinese Ceramic Society, 52*, 681–693.

Liu, M., Shafiq, M., Sun, B., Wu, J., Wang, W., El-Newehy, M., … Mo, X. (2022). Composite superelastic aerogel scaffolds containing flexible SiO_2 nanofibers promote bone regeneration. *Advanced Healthcare Materials, 11*, Article e2200499.

Liu, S., Bernhardt, A., Wirsig, K., Lode, A., Hu, Q., Gelinsky, M., & Kilian, D. (2023). Synergy of inorganic and organic inks in bioprinted tissue substitutes: Construct stability and cell response during long-term cultivation in vitro. *Composites Part B-Engineering, 261*, Article 110804.

Mao, D., Li, Q., Li, D., Chen, Y., Chen, X., & Xu, X. (2018). Fabrication of 3D porous poly (lactic acid)-based composite scaffolds with tunable biodegradation for bone tissue engineering. *Materials & Design, 142*, 1–10.

Mao, X., Shan, H., Song, J., Bai, Y., Yu, J., & Ding, B. (2016). Brittle-flexible-brittle transition in nanocrystalline zirconia nanofibrous membranes. *Crystengcomm, 18*, 1139–1146.

Mohandas, A., Deepthi, S., Biswas, R., & Jayakumar, R. (2018). Chitosan based metallic nanocomposite scaffolds as antimicrobial wound dressings. *Bioactive Materials, 3*, 267–277.

Najafabadi, B.-A.-H. M., & Abnosi, M. H. (2016). Boron induces early matrix mineralization via calcium deposition and elevation of alkaline phosphatase activity in differentiated rat bone marrow mesenchymal stem cells. *Cell Journal, 18*, 62–73.

Padalhin, A. R., Kim, B., Ventura, R. D., Lee, H. J., Lee, S. J., & Lee, B.-T. (2018). Development of fibrous balloon for facilitating the use of calcium phosphate cement in vertebral augmentation procedures. *Materials & Design, 158*, 172–183.

Porrelli, D., Gruppuso, M., Vecchies, F., Marsich, E., & Turco, G. (2021). Alginate bone scaffolds coated with a bioactive lactose modified chitosan for human dental pulp stem cells proliferation and differentiation. *Carbohydrate Polymers, 273*.

Qi, L., Fang, X., Yan, J., Pan, C., Ge, W., Wang, J., … Zhang, L. (2024). Magnesium-containing bioceramics stimulate exosomal miR-196a-5p secretion to promote senescent osteogenesis through targeting Hoxa7/MAPK signaling axis. *Bioactive Materials, 33*, 14–29.

Rabea, E. I., Badawy, M. E. T., Stevens, C. V., Smagghe, G., & Steurbaut, W. (2003). Chitosan as antimicrobial agent: Applications and mode of action. *Biomacromolecules, 4*, 1457–1465.

Ren, K., Wu, L.-H., & Xu, L. (2023). Research progress of carboxymethyl chitosan-based haemostatic materials and their haemostatic mechanism –Review. *Zhongguo Shi Yan Xue Ye Xue Za Zhi, 31*, 911–915.

Rong, S., Qi, X. U., Xiaohong, Y. U., & Shanshan, L. I. U. (2007). Antimicrobial activity of chitosan. *Food Science, 28*, 121–124.

Saravanan, S., Leena, R. S., & Selvamurugan, N. (2016). Chitosan based biocomposite scaffolds for bone tissue engineering. *International Journal of Biological Macromolecules, 93*, 1354–1365.

Su, C., Cao, Z., Liu, J., Sun, X., Qiu, K., Mu, Y., Cong, X., Wang, X., Chen, X., Jia, N., & Feng, C. (2023). The hierarchical porous structures of diatom biosilica-based hemostat: From selective adsorption to rapid hemostasis. *Journal of Colloid and Interface Science, 651*, 544–557.

Sukpaita, T., Chirachanchai, S., Pimkhaokham, A., & Ampornaramveth, R. S. (2021). Chitosan-based scaffold for mineralized tissues regeneration. *Marine Drugs, 19*, 551.

Tang, G., Liu, Z., Liu, Y., Yu, J., Wang, X., Tan, Z., & Ye, X. (2021). Recent trends in the development of bone regenerative biomaterials. *Frontiers in Cell and Developmental Biology, 9*, Article 665813.

Wang, D., Sun, Y., Zhang, D., Kong, X., Wang, S., Lu, J., Liu, F., Lu, S., Qi, H., & Zhou, Q. (2023). Root-shaped antibacterial alginate sponges with enhanced hemostasis and osteogenesis for the prevention of dry socket. *Carbohydrate Polymers, 299*, Article 120184.

Wang, F., Chen, Y., & Tan, H. (2011). Research progress of quaternary ammonium salt coupled chitosan antibacterial. *New Chemical Materials, 39*, 13–15.

Wang, K., Zhou, H., Wang, H., Li, B., & Liang, C. (2024). Bone ingrowth induced by gelatin/chitosan internal matrix of 3DP Ti6Al4V scaffold. *Biomaterials Advances, 164*, Article 213993.

Wang, L., Qiu, Y., Guo, Y., Si, Y., Liu, L., Cao, J., … Ding, B. (2019). Smart, elastic, and nanofiber-based 3D scaffolds with self-deploying capability for osteoporotic bone regeneration. *Nano Letters, 19*, 9112–9120.

Wang, X., & Chang, J. (2020). Application of bioceramics in tissue engineering. *Chinese Bulletin of Life Sciences, 32*, 257–266.

Wang, X., Yuan, Z., Shafiq, M., Cai, G., Lei, Z., Lu, Y., … Mo, X. (2024). Composite aerogel scaffolds containing flexible silica nanofiber and tricalcium phosphate enable skin regeneration. *ACS Applied Materials & Interfaces, 16*, 25843–25855.

Wang, Y., Zhang, H., Hu, Y., Jing, Y., Geng, Z., & Su, J. (2022). Bone repair biomaterials: A perspective from immunomodulation. *Advanced Functional Materials, 32*, Article 2208639.

Wei, X., Lei, L., Luo, L., Zhou, Y., Zheng, Z., & Chen, W. (2024). Advances in osteoimmunomodulation of biomaterials after intrabone implantation: Focus on surface hydrophilicity. *Journal of Materials Chemistry B, 12*, 11089–11104.

Weng, L., Boda, S. K., Wang, H., Teusink, M. J., Shuler, F. D., & Xie, J. (2018). Novel 3D hybrid nanofiber aerogels coupled with BMP-2 peptides for cranial bone regeneration. *Advanced Healthcare Materials, 7*.

Xie, X., Li, D., Chen, Y., Shen, Y., Yu, F., Wang, W., … Mo, X. (2021). Conjugate electrospun 3D gelatin nanofiber sponge for rapid hemostasis. *Advanced Healthcare Materials, 10*, Article 2100918.

Xu, J., Chang, L., Xiong, Y., & Peng, Q. (2024). Chitosan-based hydrogels as antibacterial/antioxidant/anti-inflammation multifunctional dressings for chronic wound healing. *Advanced Healthcare Materials, 13*, Article e2401490.

Xu, W., Sun, Y., Wang, J., Wang, B., Xu, F., Xie, Z., & Wang, Y. (2022). Controlled release of silibinin in GelMA hydrogels inhibits inflammation by inducing M2-type macrophage polarization and promotes vascularization in vitro. *RSC Advances, 12*, 13192–13202.

Xue, N., Ding, X., Huang, R., Jiang, R., Huang, H., Pan, X., … Wang, Y. (2022). Bone tissue engineering in the treatment of bone defects. *Pharmaceuticals (Basel), 15*, 879.

Xue, Z., Li, Y., Lu, F., & Liao, Y. (2024). Research progress of genetic engineering in promoting osteogenic differentiation of adipose-derived stem cells. *Chinese Journal of Clinical Anatomy, 42*, 233–235.

Yin, C., Jia, X., Miron, R. J., Long, Q., Xu, H., Wei, Y., … Li, Z. (2018). Setd7 and its contribution to Boron-induced bone regeneration in Boron-mesoporous bioactive glass scaffolds. *Acta Biomaterialia, 73*, 522–530.

Yuan, Z., Sheng, D., Jiang, L., Shafiq, M., Khan, A. U. R., Hashim, R., … Chen, S. (2022). Vascular endothelial growth factor-capturing aligned electrospun polycaprolactone/gelatin nanofibers promote patellar ligament regeneration. *Acta Biomaterialia, 140*, 233–246.

Yuan, Z., Zhang, L., Shafiq, M., Wang, X., Cai, P., Hafeez, A., … Xu, Y. (2024). Composite superplastic aerogel scaffolds containing dopamine and bioactive glass-based fibers for skin and bone tissue regeneration. *Journal of Colloid and Interface Science, 673*, 411–425.

Zhang, D., Huang, Z., Tong, L., Gao, F., Huang, H., Chen, F., & Liu, C. (2024). Self-restoring cryogels used for the repair of hemorrhagic bone defects by modulating blood clots. *Chemical Engineering Journal, 490*, Article 151421.

Zhang, T., Zhou, W., Jia, Z., Wei, Q., Fan, D., Yan, J., … Liu, Z. (2018). Polydopamine-assisted functionalization of heparin and vancomycin onto microarc-oxidized 3D printed porous Ti6Al4V for improved hemocompatibility, osteogenic and anti-infection potencies. *Science China Materials, 61*, 579–592.

Zhao, F., Wang, X., Ding, B., Lin, J., Hu, J., Si, Y., … Sun, G. (2011). Nanoparticle decorated fibrous silica membranes exhibiting biomimetic superhydrophobicity and highly flexible properties. *RSC Advances, 1*, 1482–1488.

Zhao, Y., Cheng, C., Wang, X., Yuan, Z., Sun, B., El-Newehy, M., … Mo, X. (2024). Aspirin-loaded anti-inflammatory ZnO-SiO_2 aerogel scaffolds for bone regeneration. *ACS Applied Materials & Interfaces, 16*, 17092–17108.

Zheng, K., Bider, F., Monavari, M., Xu, Z., Janko, C., Alexiou, C., … Boccaccini, A. R. (2024). Sol-gel derived B_2O_3-CaO borate bioactive glasses with hemostatic, antibacterial and pro-angiogenic activities. *Regenerative Biomaterials, 11*, Article 2100918.

Zheng, K., Fan, Y., Torre, E., Balasubramanian, P., Taccardi, N., Cassinelli, C., … Boccaccini, A. R. (2020). Incorporation of boron in mesoporous bioactive glass nanoparticles reduces inflammatory response and delays osteogenic differentiation. *Particle & Particle Systems Characterization, 37*, Article 2000054.

Zhou, S., He, J., Liu, Q., Chen, T., Guan, X., Gao, H., … Wu, J. (2024). Injectable hydrogel of chitosan-octyl itaconate conjugate modulates inflammatory response. *ACS Biomaterials Science & Engineering, 10*, 4823–4838.

Zhu, T., Song, X., Duan, Z., Song, Y., Hu, X., Zhou, Y., Han, Y., & Ran, X. (2024). Effects of electrostatic polarities on the morphology of electrospun oxide nanofibers: A case study on alumina-based nanofibers. *Ceramics International, 50*, 20402–20409.